Shock-wave induced instability in internal explosion dynamics

A. Bagabir and D. Drikakis
Department of Aerospace Sciences
Cranfield University
Cranfield, UK

ABSTRACT

The paper presents an investigation of flow instabilities occurring in shock-wave propagation and interaction with the walls of an enclosure. The shock-wave propagation is studied in connection with perturbed and unperturbed cylindrical blasts, initially placed in the centre of the enclosure, as well as for three different blast intensities corresponding to Mach numbers $M_s = 2$, 5 and 10. The instability is manifested by a symmetry-breaking of the flow even for the case of an initially perfectly-symmetric blast. It is shown that the symmetry-breaking initiates around the centre of the enclosure as a result of the interaction of the shock waves reflected from the walls, with the low-density region in the centre of the explosion. The instability leads to fast attenuation of the shock waves, especially for smaller initial blast intensities. The computations reveal that the vortical flow structures arising from the multiple shock reflections and flow instability are Mach number dependent. The existence of perturbations of large amplitude in the initial condition strengthens the instability and has significant effects on the instantaneous wall pressure distributions. The computational investigation has been performed using high-resolution Riemann solvers for the gas dynamic equations.

1.0 INTRODUCTION

The study of non-stationary flows featuring shock waves is motivated by the need to understand the physics of shock wave phenomena, as well as by the variety of applications in which shock waves appear spanning from engineering to astrophysics. In the case of shock (blast) wave propagation in an enclosure the interest stems from explosion dynamics which arises from the very sudden release of chemical, nuclear, electrical or mechanical energy in a limited space.

Even though past studies have investigated instabilities occurring when two fluids of different densities are impulsively accelerated into each other by a shock wave, known as Richtmyer-Meshkov (or impulsive Rayleigh-Taylor) instability[6,18], the investigation of flow instabilities arising from the interaction of blast waves with a solid structure has received scarce attention. Flow instabilities have been experimentally detected in the case of cylindrical blast waves[7,14]. Burrows and Fryxell (1992)[5] have also shown that instabilities can occur in the mantles of nascent neutron stars implying that the standard spherically symmetric models of neutron star birth and supernova explosion may be inadequate. The above findings follow earlier analytical work[4] regarding the formation of convective

Paper No. 2982. Manuscript received 26 May 2005, revised version received 5 August 2005, accepted 30 August 2005.

https://doi.org/10.1017/S0001924000000890 Published online by Cambridge University Press

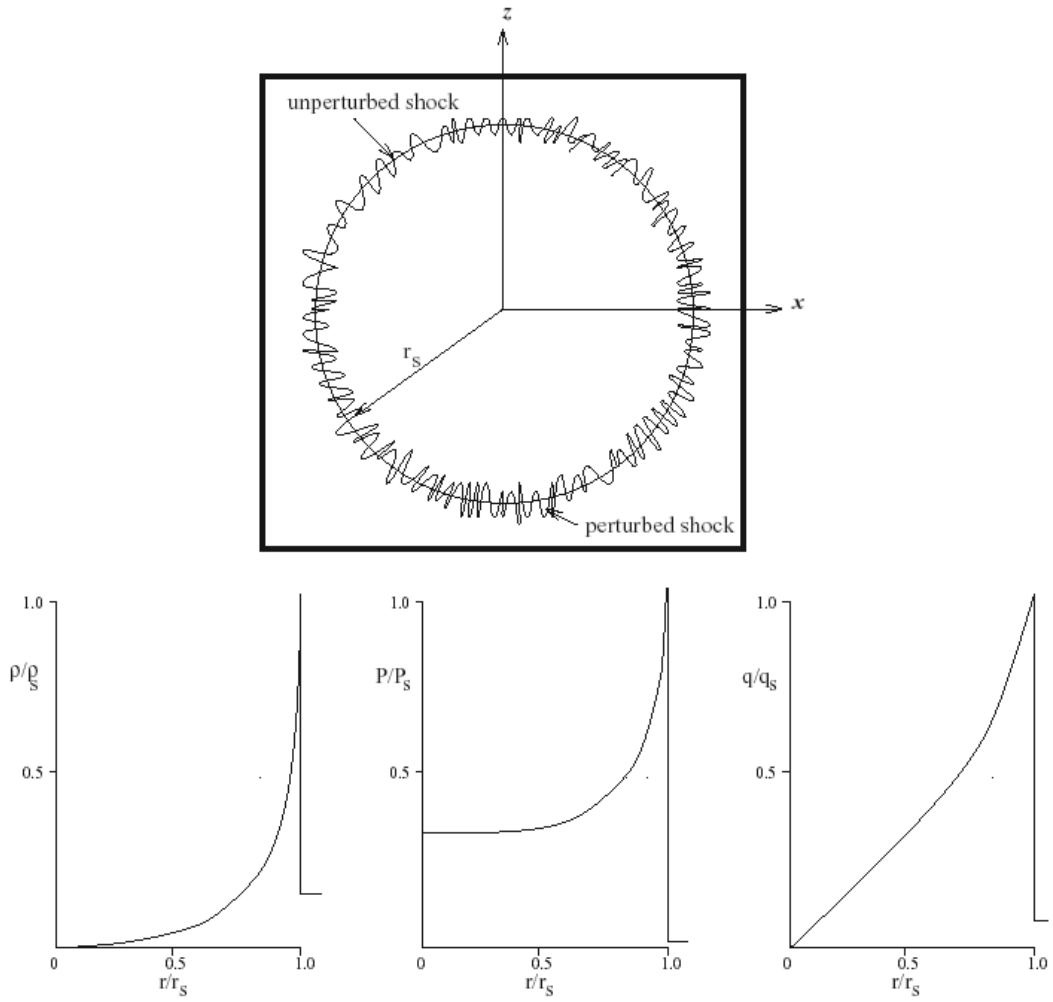


Figure 1. Geometry of the blast-wave problem, as well as density, pressure and velocity profiles used as initial conditions.

instabilities in spherical ideal gas expansion. Furthermore Marconi[15] performed a numerical investigation of the propagation of a blast wave of in an enclosure and detected the formation of instability following the reflection of the blast wave from the walls of the structure.

Because of the lack of detailed experiments for internal explosions, numerical simulations provide an alternative for studying complex shock physics in these flows. In the present work, the problem set-up is the same as that employed by Marconi[15]. This consists of an enclosure in which an explosion takes place around its centre (Fig. 1). A very hot region is formed at the centre of the explosion, of very low density and finite pressure, which slowly expands as time goes on. It is known that when two fluids of different density are impulsively accelerated into each other by a shock wave and when at the same time the interface separating them is not perfectly flat, a shock-excitation occurs known as Richtmyer-Meshkov (or impulsive Rayleigh-Taylor) instability.

In the case of the enclosure shown in Fig. 1, the onset of instability occurs after reflection of the shock waves from the walls as well as multiple shock interactions around the centre of the enclosure. This instability has similarities with the one arising during the interaction of shock waves with gas-inhomogeneities[6,18]. In the present case, the interest to study the flow instability stems both from the fundamental and the application point of view. The latter emerges from the need to accurately predict the pressure loads on the walls of a structure and, subsequently, design the structure's resistance against explosive loads. The objectives of the present investigation are: (*i*) to study the onset of symmetry-breaking and associated instabilities for three different cases namely an initially cylindrical symmetric blast as well as two cases of initially asymmetric blasts of increasing perturbation amplitudes; (*ii*) to investigate Mach number effects for the above cases; (*iii*) to examine the effects of the instability on the wall pressure loads for different Mach numbers and perturbation intensities; and (*iv*) to examine the effects of multiple shock reflections and symmetry-breaking on the vorticity generation. The investigation has been performed using high-resolution Riemann solvers in conjunction with an implicit time integration method.

The remainder of the paper is organised as follows. Section 2 summarises the computational strategy. Section 3 describes the problem set-up and discusses the results. Section 4 summarises the conclusions of the present study.

https://doi.org/10.1017/S0001924000000890 Published online by Cambridge University Press

2.0 COMPUTATIONAL MODELLING

The computational study is based on the two-dimensional inviscid gas dynamic equations. Previous investigations pertinent to Richtmyer-Meshkov instability under various flow conditions, e.g. shock/density-interface interaction[16], blast wave propagation in an enclosure[15] and flows in astrophysics[5], have also employed a similar computational set-up. The above studies have shown that although a two dimensional model cannot represent three-dimensional effects on the small-scale processes, insight in relation to a number of physical phenomena can still be gained on the basis of two-dimensional simulations. In the present case these phenomena include the spatial-temporal onset of symmetry-breaking as a function of the blast intensity; qualitative features regarding the enhancement of the instability due to the presence of perturbations; as well as the effects of the instability on the wall pressure distributions.

The two-dimensional Euler equations for a compressible fluid are written in a matrix form and curvilinear co-ordinates (ξ,ζ) as

$$\frac{\partial Q}{\partial t}+\frac{\partial E}{\partial \xi}+\frac{\partial G}{\partial \varsigma}=0 \qquad \ldots (1)$$

The matrix; $$\mathbf{Q}=J\left(\rho,\rho u,\rho w,e\right)^{T}=JU^{T} \qquad \ldots (2)$$

contains the conservative variables:
where ρ is the density, u and w are the velocity components, e is the total energy per unit volume, and J stands for the Jacobian of the transformation from Cartesian (x,z) to curvilinear (ξ,ζ) co-ordinates. The inviscid fluxes E, G are written as:

$$\mathbf{E}=J\begin{pmatrix}\rho U\\ \rho u\tilde{U}+p\xi_x\\ \rho w\tilde{U}+p\xi_z\\ (e+p)\tilde{U}\end{pmatrix}\quad \mathbf{G}=J\begin{pmatrix}\rho\tilde{W}\\ \rho u\tilde{W}+p\zeta_x\\ \rho w\tilde{W}+p\zeta_z\\ (e+p)\tilde{W}\end{pmatrix} \qquad \ldots (3)$$

with

$$\tilde{U}=u\xi_x+w\xi_z,\quad \tilde{W}=u\zeta_x+w\zeta_z \qquad \ldots (4)$$

The geometry of Fig. 1 does not require the use of curvilinear co-ordinates, but the computational code has been developed to handle any arbitrary geometric shape using body-fitted co-ordinates thus the equations are solved in the above form. The pressure, p, is calculated by the ideal gas equation of state, $p=\rho(\gamma-1)i$, where γ is the ratio of specific heats ($\gamma=1{\cdot}4$) and i is the internal energy.

In order to reduce uncertainties associated with the numerics, three different methods were implemented in the computations: Roe's Riemann solver[16,17]; the CBM-FVS scheme, where the discretisation of the inviscid fluxes is obtained by a combination of a Riemann solver (characteristics-based scheme) of (Eberle & Heiss 1993)[10] and a flux vector splitting (FVS) scheme (Zóltak and Drikakis 1998)[25]; and the HLLC Riemann solver of Toro *et al*. (1994)[21]. These schemes as well as the time integration algorithm are described in the Appendix.

3.0 RESULTS

3.1 Problem description

The problem set-up is schematically shown in Fig. 1. An explosion is initiated at the centre of a square enclosure and a cylindrical blast wave moves into a gas at rest of ambient density and pressure of $1{\cdot}21\text{kg/m}^3$ and $1{\cdot}013\text{bar}$, respectively. The enclosure is a square and the unperturbed, perfectly symmetric blast has been obtained considering that the flow is essentially cylindrical before the blast interacts with the walls[15,19]. To generate the initial cylindrical blast, the one-dimensional gas dynamic equations in cylindrical form are solved for an arbitrary strong shock running into a gas at rest. The pressure and density were assumed constant at their shock values in the region between the shock and the blast origin. The hot region at the centre of the explosion, encompassing very low density and finite pressure, slowly expands as time goes on. The radial velocity is linearly decreased from its shock value to zero at the origin (Fig. 1). After an initial startup period all the variables approach a self-similar variation[19] between the origin and the shock. The density (ρ/ρ_s), pressure (p/p_s) and velocity (q/q_s), (where q is the total velocity $\sqrt{u^2+v^2}$ and q_s the radial velocity of the initial shock) profiles are shown in Fig. 1. These profiles are non-dimensionalised using the corresponding shock values and are used as initial conditions in the case of a perfectly symmetric blast, henceforth labelled as case S (symmetric). The initial data was modified by assigning area-weighted values to the appropriate computational cells at the initial time ($t=0$). This procedure avoids the formation of small amplitude waves created at early times as a result of the staircase configuration of the data.

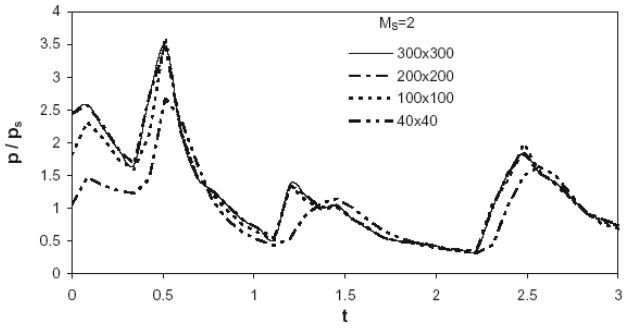


Figure 2. Comparison of maximum wall pressure (normalised by the shock pressure p_s) for different grid resolutions.

Since in the reality the blast will never be perfectly symmetric, the flow was also studied for the case where random (non-periodic) perturbations of large amplitude are imposed on the initial blast. The perturbations are applied in the region between the origin of the explosion ($r=0$) and the outer shock position ($r=r_s$). Considering a perturbation with average amplitude η_o and wavelength λ_p, results are presented here for two different initial perturbations corresponding to values $2\pi\eta_0/\lambda_p=3{\cdot}3$ (henceforth labelled P1 case) and $6{\cdot}6$ (henceforth labelled $6{\cdot}6$ case), respectively. The perturbation amplitudes were defined as in the experiment of Houas *et al* 1988[13] for the shock-induced Rayleigh-Taylor (or Richtmyer-Meshkov) instability that develops between two fluids of different densities. Note that the present flow problem is different than the classical problem of Richtmyer-Meshkov instability because the interface (including the perturbed case scenario) that separates the two regions of different density is created as the result of the explosion. This interface problem cannot be directly related to the theoretical and experimental investigations of RM instability, where a shock-wave refracts through a (prescribed) perturbed interface separating two different gases, however, both problems share similarities. In the course of this investigation, several other perturbation amplitudes were also considered, but the results presented below were found to be the most representative to explain the effects of large perturbations on the development of instability and wall pressure loads. The shock wave instability was studied for three different shock Mach numbers (M_s) of 2, 5 and 10.

For the numerical methods employed here, a Cartesian grid 300×300 was found sufficient for providing grid independent solutions for the wall pressure distributions and the onset of instability (details are presented in Section 3.3). The time variation of the maximum

https://doi.org/10.1017/S0001924000000890 Published online by Cambridge University Press

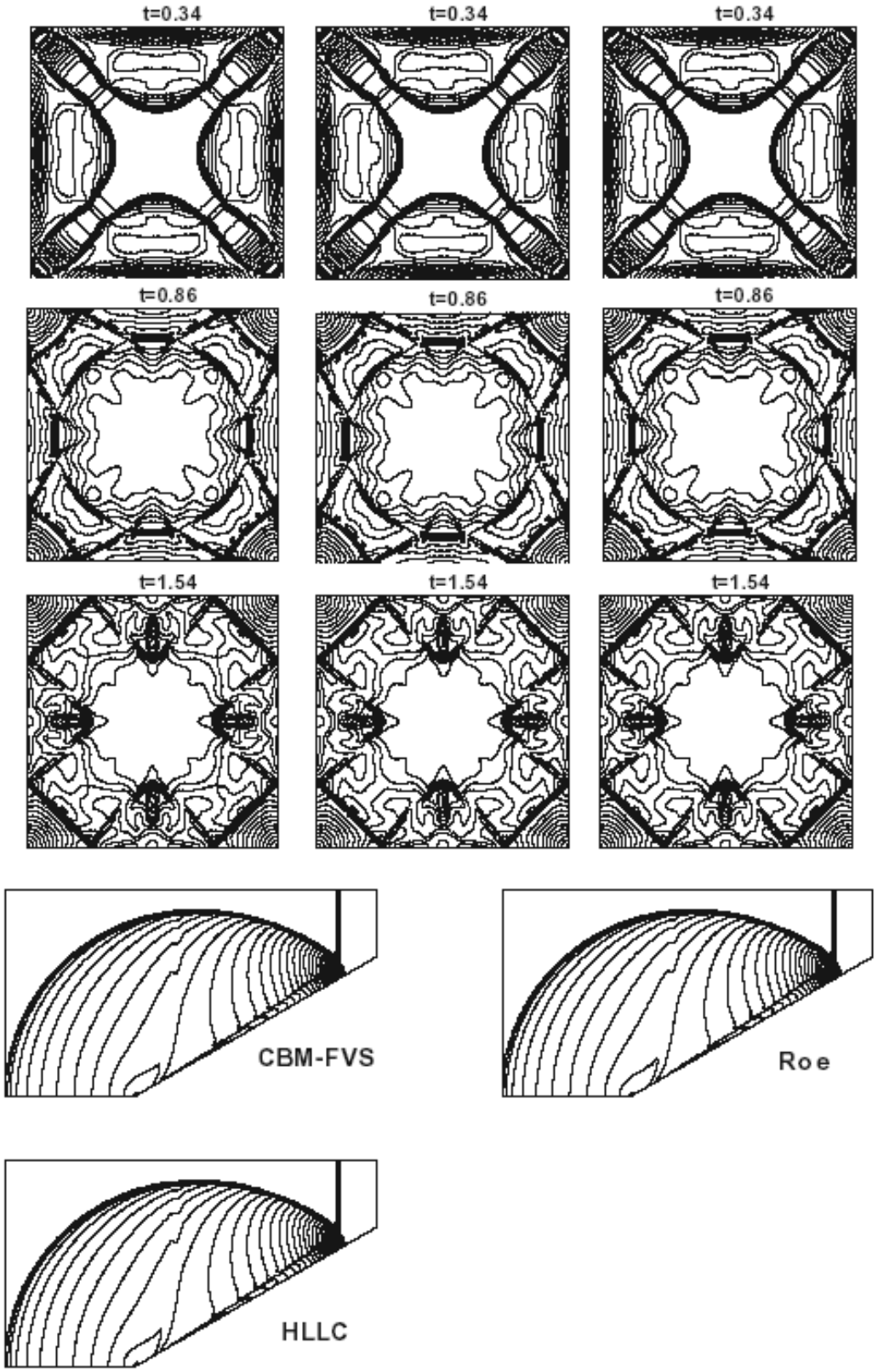


Figure 3. Comparison of flow patterns (iso-density contours) as obtained by different numerical schemes for the shock-box interaction problem: CBM-FVS (left column), Roe (middle), HLLC (right column); and for shock-wedge diffraction (bottom plots).

https://doi.org/10.1017/S0001924000000890 Published online by Cambridge University Press

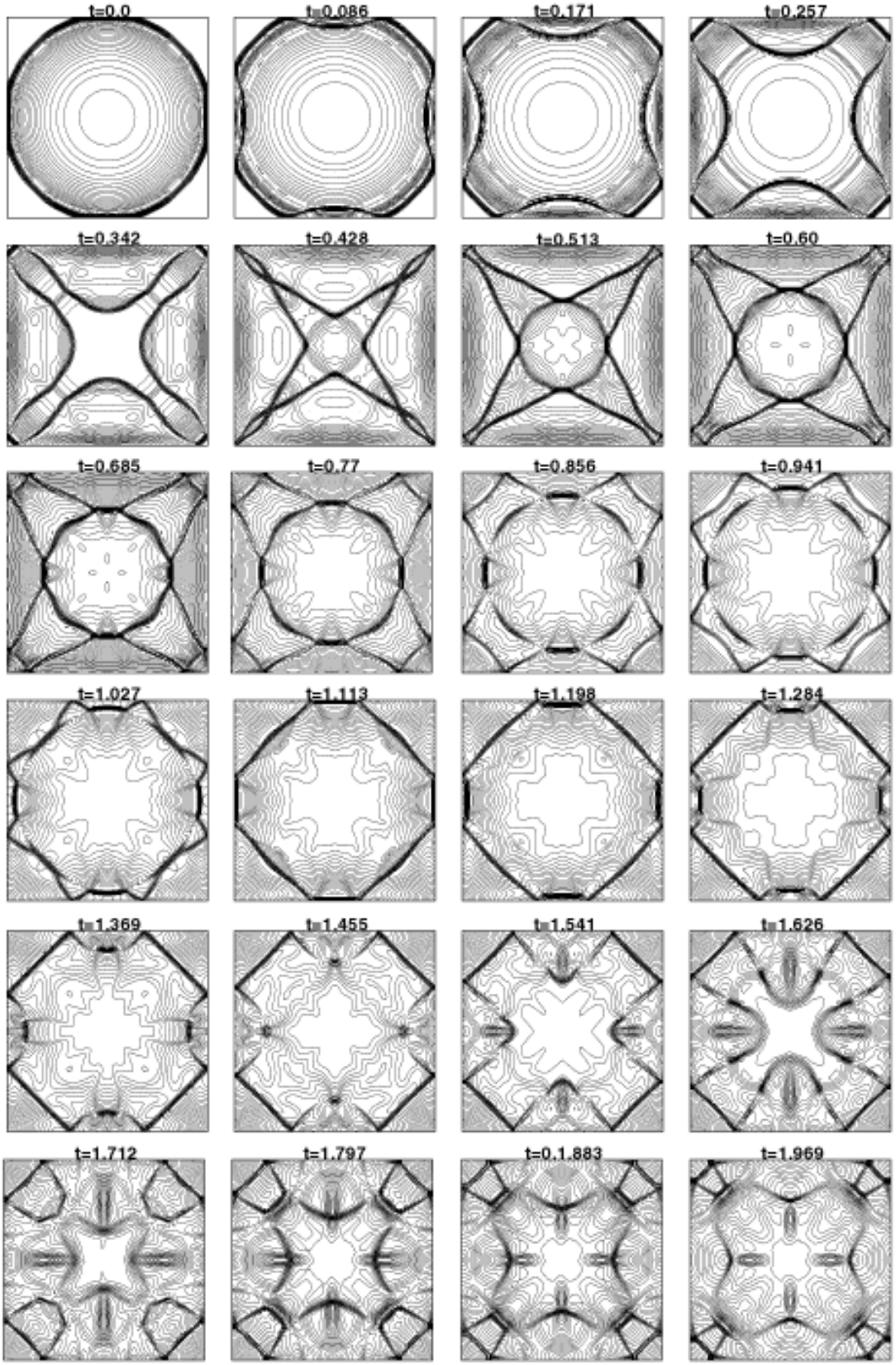


Figure 4. Mach number contours for the symmetric blast wave (case *S*) at $M_s = 2$; the frames have been plotted using a dimensionless time step, $\Delta t = 0{\cdot}0855$ (continued).

https://doi.org/10.1017/S0001924000000890 Published online by Cambridge University Press

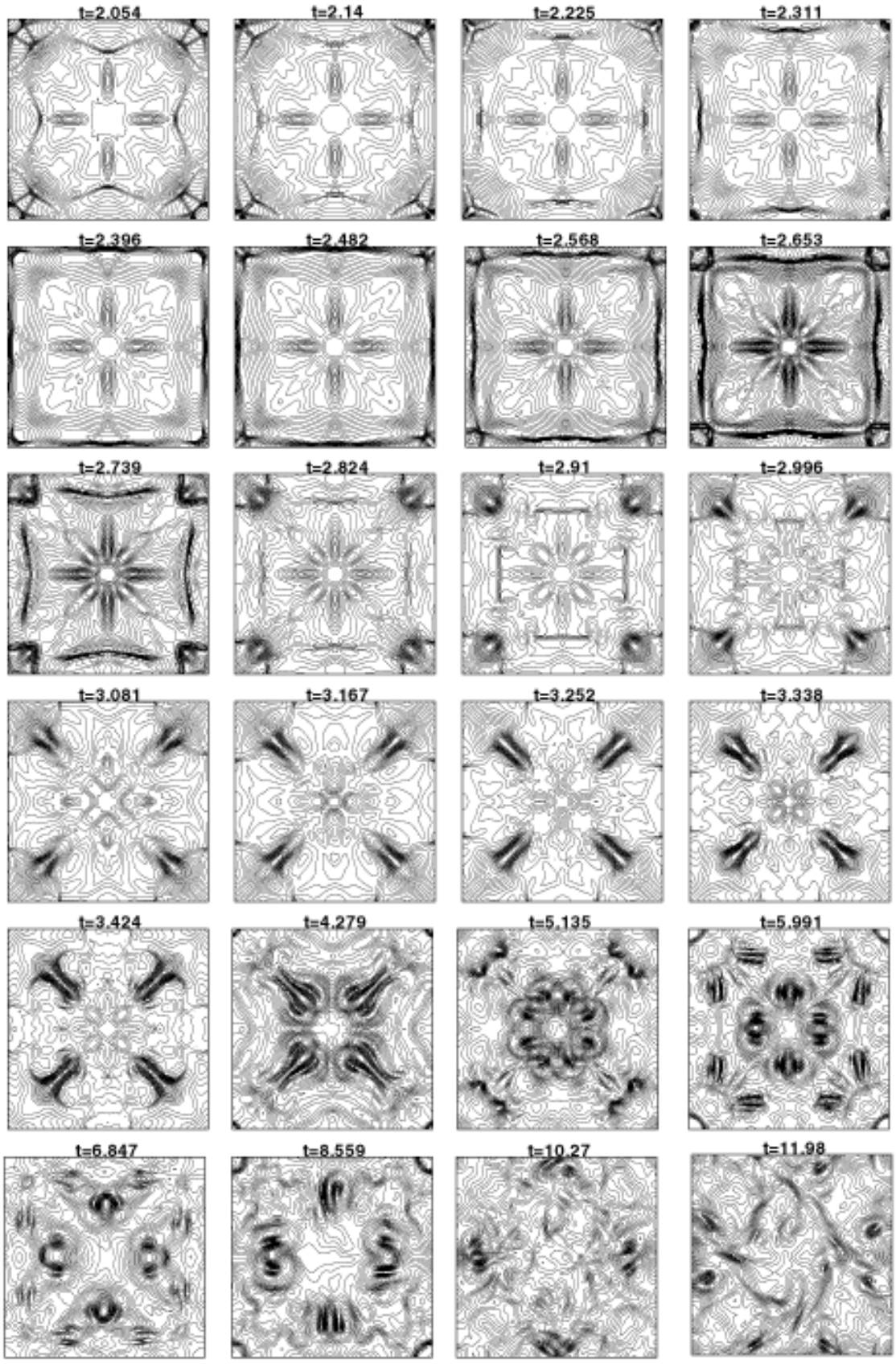


Figure 5. Mach number contours (continued from Figure 4) for the symmetric blast wave (case S) at $M_s = 2$; the frames have been plotted using a dimensionless time step $\Delta t = 0{\cdot}0855$ except for the last two rows where $\Delta t = 0{\cdot}855$.

https://doi.org/10.1017/S0001924000000890 Published online by Cambridge University Press

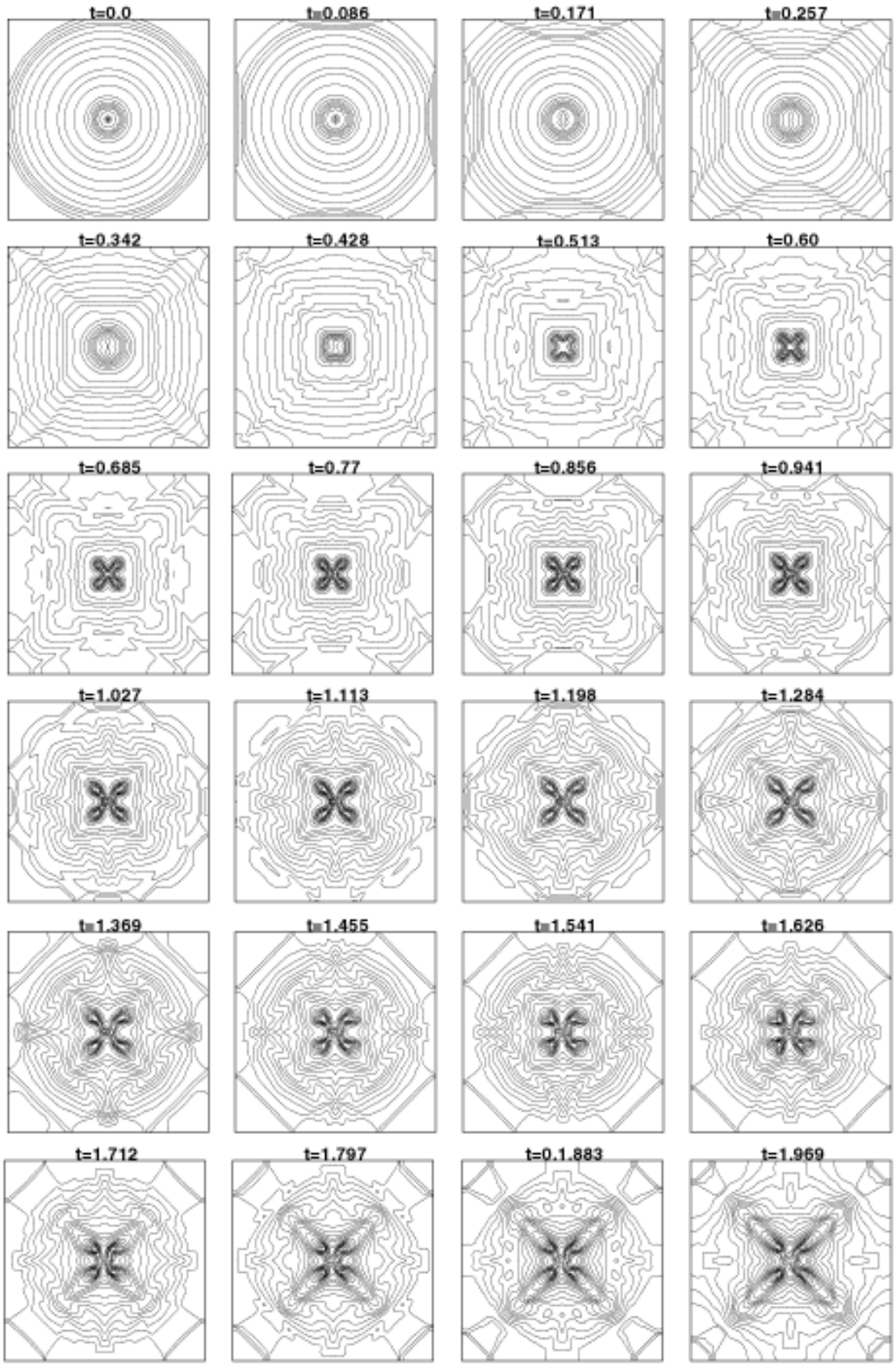


Figure 6. Density ln(ρ) dimensionless based on ρ_s, contours for the symmetric blast wave (case S) at , $\Delta t = 0{\cdot}0855$ (continued).

https://doi.org/10.1017/S0001924000000890 Published online by Cambridge University Press

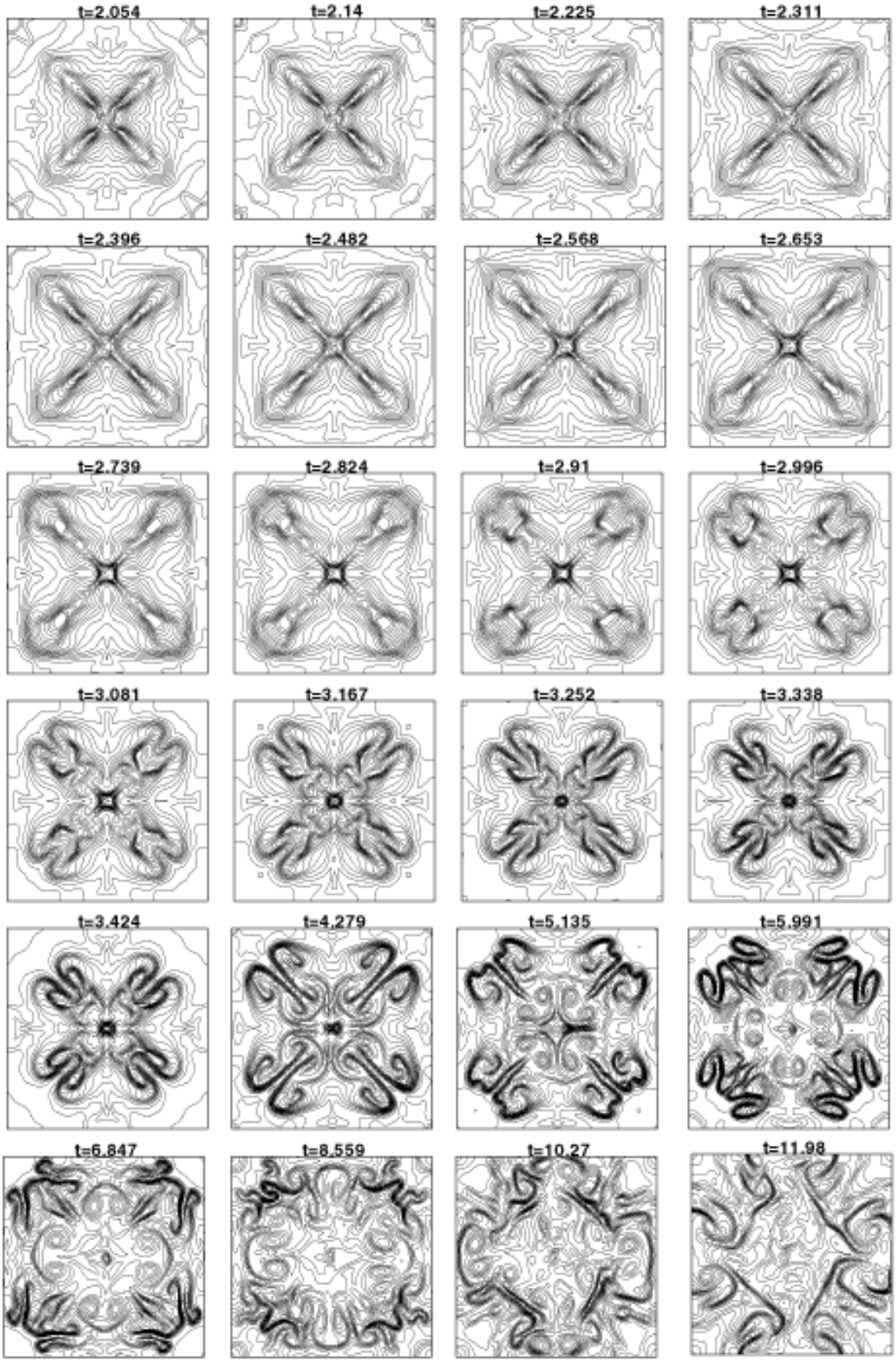


Figure 7. Density ln(ρ) contours for the symmetric blast wave (case S) $M_s = 2$; $\Delta t = 0{\cdot}0855$ except for the last two rows, where $\Delta t = 0{\cdot}855$.

https://doi.org/10.1017/S0001924000000890 Published online by Cambridge University Press

wall pressure load occurring around the box for $M_s = 2$ is shown in Fig. 2 using different grid resolutions. The time, t, has become dimensionless using the shock velocity and the maximum radius of the shock (r_s). Fig. 2 shows that the results for the grids 200×200 and 300×300 are almost identical. In the same figure, the pressure variations show that the three schemes provide the same results for the pressure variation. It was also found that these numerical schemes provide the same flow patterns and this conclusion was verified for all the flow cases considered here. In Fig. 3 the Mach number contours at three different time instants are compared for the Roe, HLLC and CBM-FVS Riemann solvers (details are discussed below). The similarities in the solutions obtained by the above three Riemann solvers were also verified in (Bagabir and Drikakis 2001; 2004)[1,2] for several different unsteady flow cases. In Fig. 3 we (indicatively) show the solutions that have been obtained using the above high-resolution schemes for the shock-wedge diffraction problem. This problem is described here by an incident shock wave ($M_s = 1{\cdot}2$), initially perpendicular to the x direction, encountering a wedge at an angle of 30°. There is a number of shock-wave reflection phenomena which may appear depending on the incident Mach number and the wedge-angle, e.g., regular, single, complex, and double Mach reflection. Comprehensive discussion on these phenomena can be found in (Ben-Dor 1992[3]; Dewey 1992[8]; Takayama 1995[20]). We performed computations on a 420×240 grid, which is the same with one used in (Toro 1999)[22]. The solution corresponds to a single Mach reflection[3,8,20] according to which the three shocks, the incident, reflected and Mach stem, meet at the triple point. A contact surface emerges from the triple point that joins the wedge surface at a sharp angle. The present results were found in very good agreement with other numerical results (see iso-density contours in (Toro 1999, pages 591-592[22]).

In addition to the above three solvers, the original versions of the HLLC (i.e., the Harten-Lax-van Leer scheme known as HLL) and FVS schemes were also employed at the initial stages of the investigation. Both schemes were found to suppress the instability even for higher mesh resolutions. This is likely to be due to the dissipative behaviour exhibited by these schemes.

3.2 Shock-wave instability at different Mach numbers

Using the CBM-FVS scheme, investigations of both perturbed and unperturbed blasts were conducted. The Mach number effects are discussed in detail in Section 3.4. Computations were initially performed for an unperturbed (symmetric) shock of Mach number $M_s = 2$. Figures 4 and 5 show the Mach contours at different time instants. These results were plotted using a dimensionless† time step $\Delta t = 0{\cdot}0855$ except for the last two rows of Fig. 5 in which $\Delta t = 0{\cdot}855$. The corresponding density contours are shown in Figs 6 and 7, respectively. The Mach contours show the shock system more clearly than the density contours. The first frame in Fig. 4 corresponds to the time instant where the cylindrical blast comes in contact with the walls for first time, which is considered to be the time $t = 0$.

The following four frames of Fig. 4 show four concave shock segments reflecting from the four walls and moving back towards the center of the explosion. The shock segments spread towards the corners of the enclosure. At $t = 0{\cdot}428$, the reflected shock has reached the exploded expansion wave at the centre and leads to a new cylindrical blast wave, which explodes towards the walls as time progresses. The shock waves produced from the corners start moving towards the center of the explosion ($t = 0{\cdot}685$). The shock-shock interactions appear to form octagon-shape shocks at $t = 1{\cdot}113$. Another shock focusing event then occurs between $t = 1{\cdot}113$ and $t = 1{\cdot}541$, the four polygons of the pentagon-shaped shocks adjacent to the walls are imploding towards the center to produce four strong shocks of arrow shape. These arrow-shape shocks interact with the contact surface at the centre ($t = 1{\cdot}712$) and pass through the low density region ($t = 1{\cdot}797$).

† The normalisation is based on sM_s/r_s, where s is the speed of sound, M_s the shock wave Mach number and r_s the shock radius.

As shown in the first and second rows of Fig. 5, the transmitted shocks meet eventually at the deformed hot core. During the blast propagation, the centre of explosion experiences several wave interactions and its shape is constantly modified by the flow. The third and forth rows of Fig. 5 show the development of four corner shocks, which interact diagonally with the low density region. The third interaction excites the flow field further resulting in stronger asymmetries as time goes on. This unstable flow behaviour is a result of the multiple shock interaction around the centre of explosion. This interaction takes place after the shock segments reflect from the four walls and reach the low density region (inferred from Fig. 6) around the centre of the enclosure.

One would expect that the flow field will maintain a quarter plane symmetry as the initial and boundary conditions are symmetric about the diagonals of the square. However, the results reveal that a symmetry-breaking starts to appear clearly at the centre of the enclosure at approximately time ($t = 2{\cdot}054$) The asymmetric pattern is attributed to the Richtmyer-Meshkov (impulsive Rayleigh-Taylor) instability because its formation is a result of the shock wave interactions with the low density region at the centre.

The density (ρ) contours shown in Figs 6 and 7 show the development of the Richtmyer-Meshkov instability. The first two rows of Fig. 6 reveal that the centre of the explosion forms a contact surface with a discontinuity in density, which deforms in time according to the compression and expansion waves. The first interaction of the shock waves with the low density region at the centre ($t = 0{\cdot}428$) forms four diagonal vortex spikes connected to the centre by thin vortical sheets. The vortices grow slowly until the second shock interaction occurs at the centre (starting at $t = 1{\cdot}626$)). As time progresses, the vortices grow up further and eventually roll up into mushroom-shaped spikes which characterise the Richtmyer-Meshkov instability (see $t = 4{\cdot}279$ of Fig. 7).

The investigation was also performed for different blast intensities. The Mach contours for the blast of $M_s = 10$ are shown in Fig. 8, where the frames have been plotted using a large (dimensionless) time step $\Delta t = 1{\cdot}43$ in order to reveal the asymmetries after the simulation has evolved for long time. Similar to $M_s = 2$, Fig. 8 shows the development of the Richtmyer-Meshkov instability at $M_s = 10$ for the case of a perfectly symmetric blast.

3.3 Onset of the symmetry breaking

Investigation of the onset of the instability was carried out by monitoring the velocity differences (for the symmetric case) in positions (see Fig. 9) symmetrically located around the enclosure centre. Figures 10 and 11 show the velocity difference between positions 1 and 2 at different Mach numbers. The velocity differences between positions 5 and 8 as well as 6 and 7 are shown in Fig. 12, while the velocity difference between 1 and 3 is shown in Fig. 13. When no instability exists the velocity differences are equal to zero and deviate from this value as the instability further develops. Figures 10 and 11 show that the velocity difference becomes larger at later times (Fig. 11) when the instability has been clearly developed in the flow field. In Figs 10-13, the arrows indicated by the numbers 2 and 3 show the time when the second and third wall reflections, respectively, occur. The onset of the instability occurs before the second wall reflection, as the shock waves move towards the walls and after they have interacted around the enclosure centre (Fig. 12).

The onset of instability takes place around the centre where the shocks interact with the low density region. This can be seen by comparing the velocity differences in the various selected positions. The difference ΔU_{67} (Fig. 12) starts to deviate from zero earlier than the velocity differences in the other positions (see Figs 10-13). Moreover, the instability initiates around the same dimensionless time, t, for all Mach numbers considered here.

The results for $M_s = 5$ and 10 (Figs 10, 11 and 13) indicate that after the third wall reflection the velocity differences are significantly

https://doi.org/10.1017/S0001924000000890 Published online by Cambridge University Press

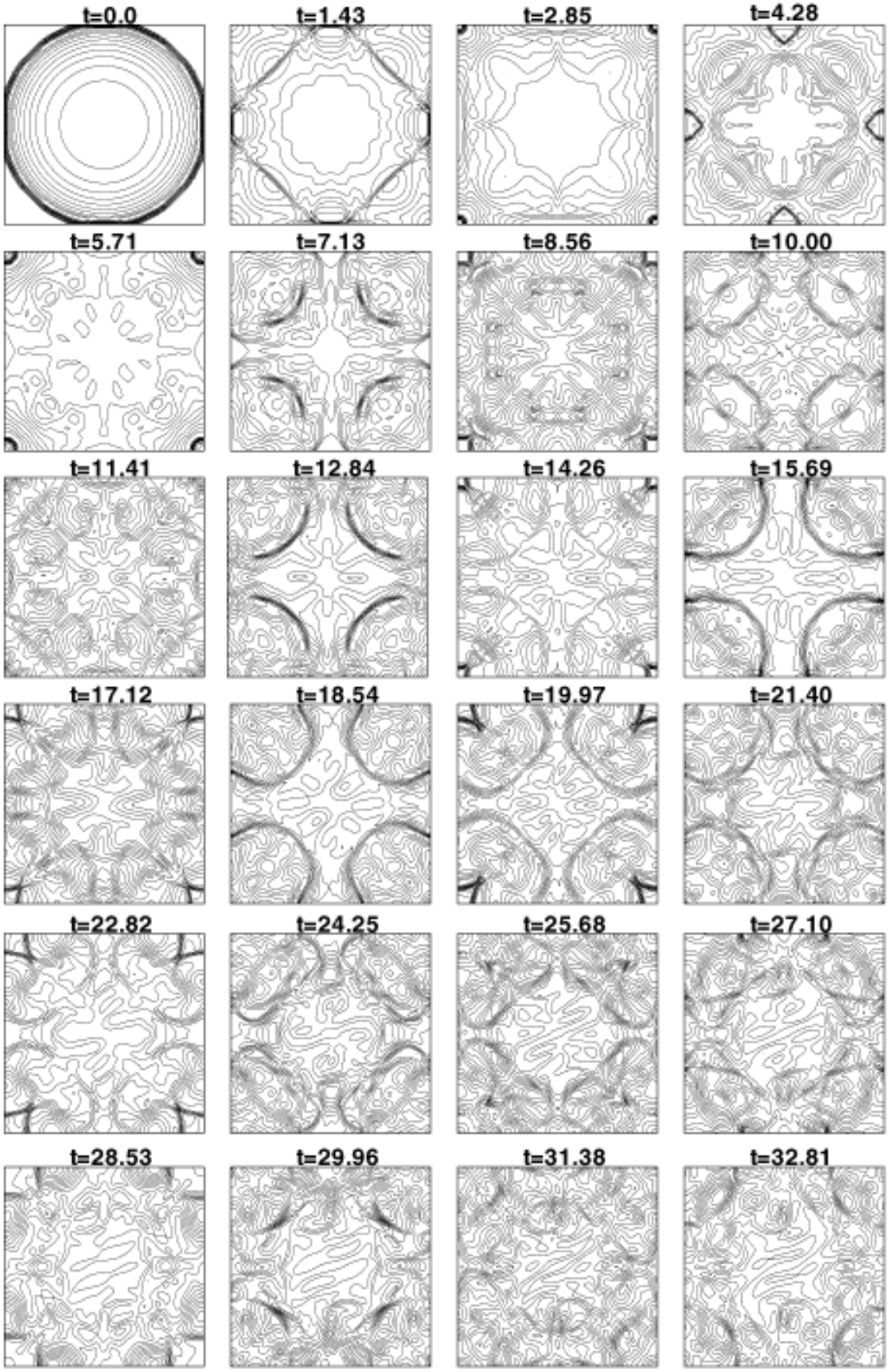


Figure 8. Mach number contours for the symmetric blast wave (case S) at $M_s = 10$; $\Delta t = 1{\cdot}43$.

https://doi.org/10.1017/S0001924000000890 Published online by Cambridge University Press

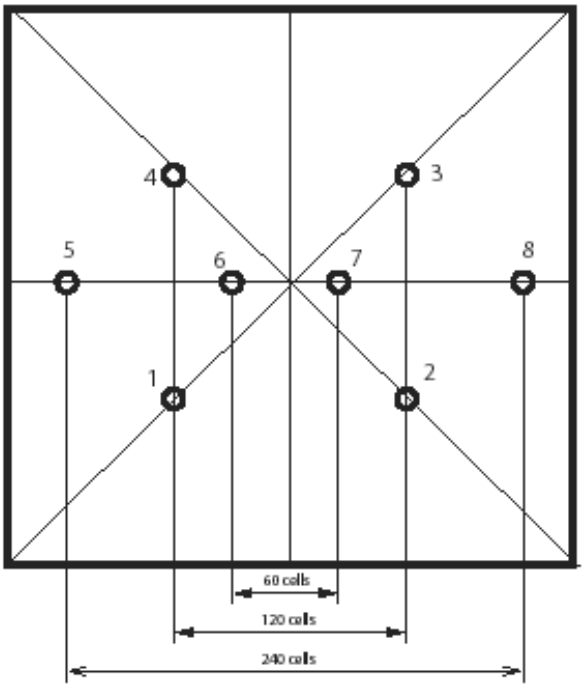


Figure 9. Selected locations for monitoring the velocity difference.

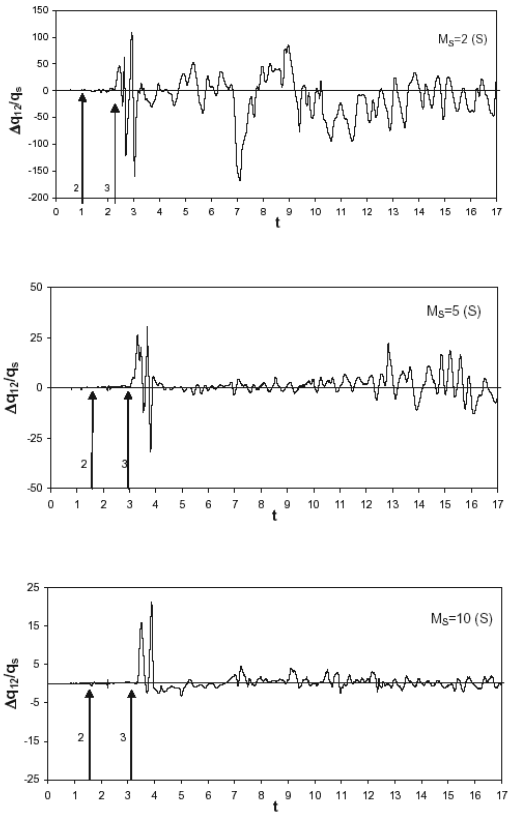


Figure 10. Velocity difference between points 1 and 2 (see Fig. 9) as function of time (time interval $t = 0 - 17$). The velocity q is defined by $q = \sqrt{u^2 + v^2}$; q_s is the radial velocity at the shock.

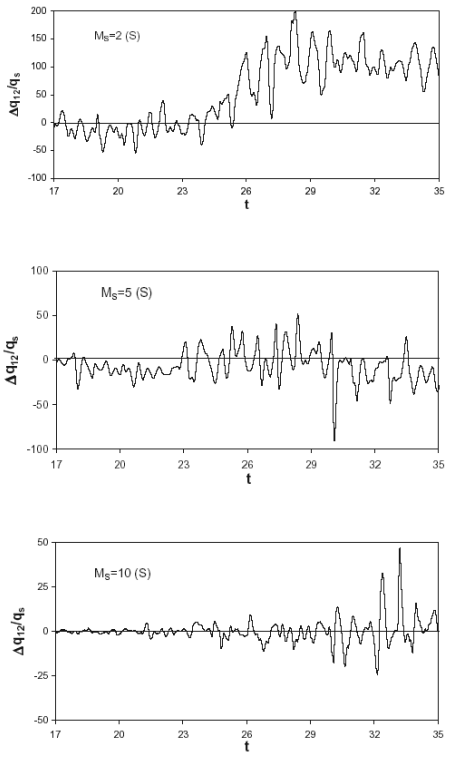


Figure 11.Velocity difference between points 1 and 2 (see Fig. 9) as function of time (time interval $t = 17 - 35$).

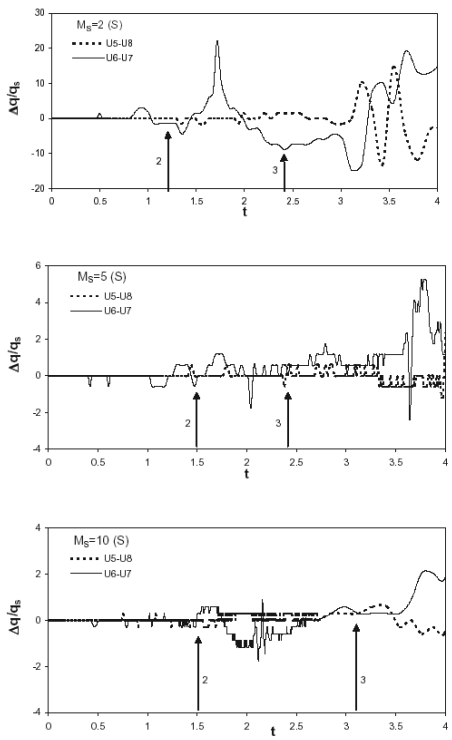


Figure 12. Velocity difference between points 5 and 8, as well as, 6 and 7 (see Fig. 9) as function time.

https://doi.org/10.1017/S0001924000000890 Published online by Cambridge University Press

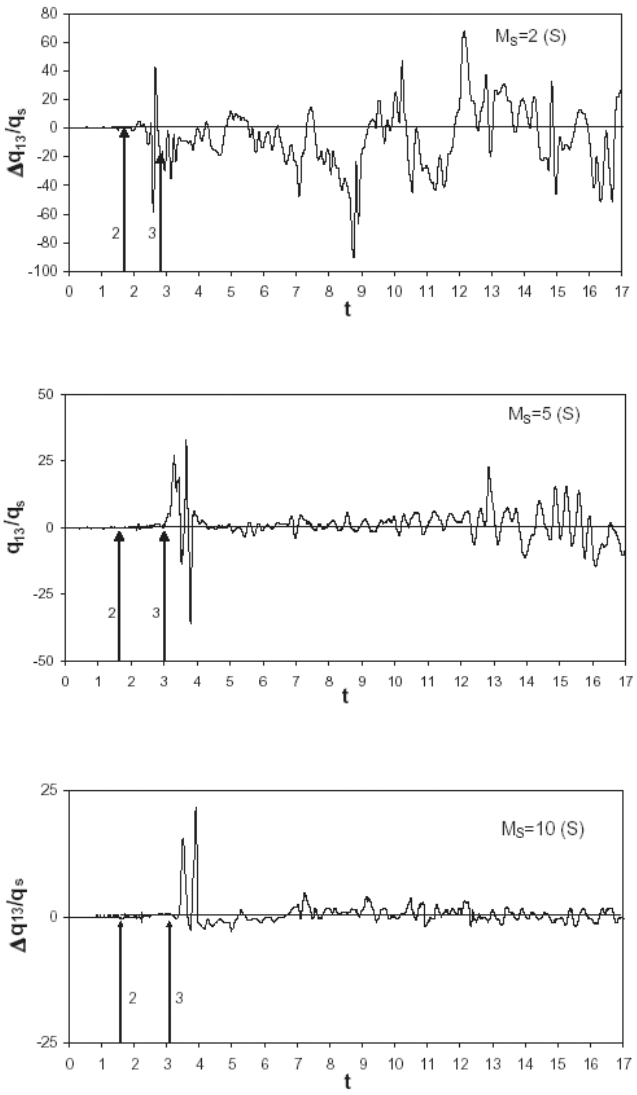


Figure. 13. Velocity difference between points 1 and 3 (see Fig. 9) as function of time.

reduced compared to M_s = 2 case, fluctuating around the zero value (stabilisation) for a certain time interval. The stabilisation lasts longer for the case of M_s = 10 than M_s = 5, while it does not appear for M_s = 2. The above can be considered as a tendency of the flow to return to 'stable' conditions, for the case of the strong blast, after the onset of the instability occurs. This 'restabilising' behaviour was found to appear locally away from the enclosure centre. A similar 'restabilising' behaviour was also found when perturbations were imposed (plots not shown here), but in this case the flow field was more difficult to return to or sustain for long enough a stable-like behaviour.

3.4 Direct comparison of blasts of different intensity

Comparison of the flow development for three different Mach numbers M_s = 2,5 and S, P1 for the cases S, P1, and P2 are shown in Figs 14, 15 and 16, respectively. The computations show the effects of the blast intensity on the development of the instability with and without the presence of random perturbations. The plots in the first, second and third rows correspond to the first, second and third shock reflections, respectively, around the centre. The flow fields for M_s = 5 and 10 are quite similar up to the third multiple shock interaction (t = 3·4), while larger differences occur between these two Mach numbers and the case of M_s = 2. For M_s = 2,5 large asymmetric flow patterns clearly appear after t = 4·3 and these are profound around the centre of the enclosure. At t = 12·8 the instability has resulted in large asymmetric flow patterns, especially for M_s = 2 and M_s = 5 (Fig. 14). Around the same time the instability has resulted in the attenuation of the entire shock system for M_s = 2, while it has also initiated a significant distortion of the shocks for M_s = 5. On the other hand, for M_s = 10 the structure of the shock system is sustained longer.

When perturbations are imposed (Figs 15 and 16) the asymmetries develop faster. For all Mach numbers and perturbation amplitudes considered here, these asymmetries initiate away from the shock waves and penetrate the shock system later. This can be seen even at the early stages of the flow development (plots in the first row of Figs 15 and 16), where the shock waves remain intact for M_s = 5 and 10. In the perturbed flow cases the asymmetries are larger around the centre of the enclosure especially at the early time instants. The cases P1 and P2 are also discussed in more detail below with respect to the vorticity field and pressure distributions.

3.5 Vorticity field

The multiple shock reflections and interactions are also associated with the generation of positive and negative vorticity regions. The vorticity field, *curl(u)*, (made dimensionless using the shock velocities at the incident Mach number M_s and the length of the box) at different Mach numbers is shown in Figs 17, 18 and 19 for the cases S, P1, and P2, respectively. The maximum and minimum vorticity values are given above each plot, where the negative vorticity is represented by dashed contour lines. The various plots correspond to the dimensionless time instants shown in Figs 14, 15 and 16.

Concerning the symmetric case, *S*, (Fig. 17), similarities exist in the vorticity fields of M_s = 5 and M_s = 10. The vorticity field for M_s = 2 evolves slightly differently. In all cases, elongated structures of positive and negative vorticities are initially formed along the centre lines of the enclosure with their extreme positive and negative values occurring around the centre. For higher Mach numbers the elongated structures appear even at later time instants (see the last two rows in Fig. 17), whereas for M_s = 2 circular structures gradually replace entirely the elongated ones. Circular structures also appear locally for M_s = 5 and 10 (see the 3rd, 5th and 6th frames in Fig. 17) and co-exist with the elongated pairs of positive-negative vorticity. However, for these Mach numbers the circular structures significantly increase, at later times, compared to the case of M_s = 2 (frames not shown here). In general, the elongated structures were found to be associated with the presence of strong shock waves, whereas the circular ones emerge when the shock waves have been significantly attenuated.

The vorticity is, generally, larger for M_s = 2 than the other two Mach numbers. It appears to be associated with the large disturbances in the flow field that are established earlier in time for the case of M_s = 2 compared to M_s = 5 and 10. The same also occurs when perturbations are applied (cases P1 and P2 in Figs 18 and 19, respectively). The perturbations result in large vorticity values during the first shock interaction around the centre of the enclosure (compare the first and second frames in Figs 18 and 19 with the corresponding ones in Fig. 17).

Increasing the perturbation amplitude tends to modify the form of the vortical structures from elongated to circular ones. It seems that the formation of the circular structures is associated with the enhancement of the instability (large asymmetric flow patterns), weakening of the shock waves (due to multiple shock interactions), and also significant mixing between different flowfield regions at

https://doi.org/10.1017/S0001924000000890 Published online by Cambridge University Press

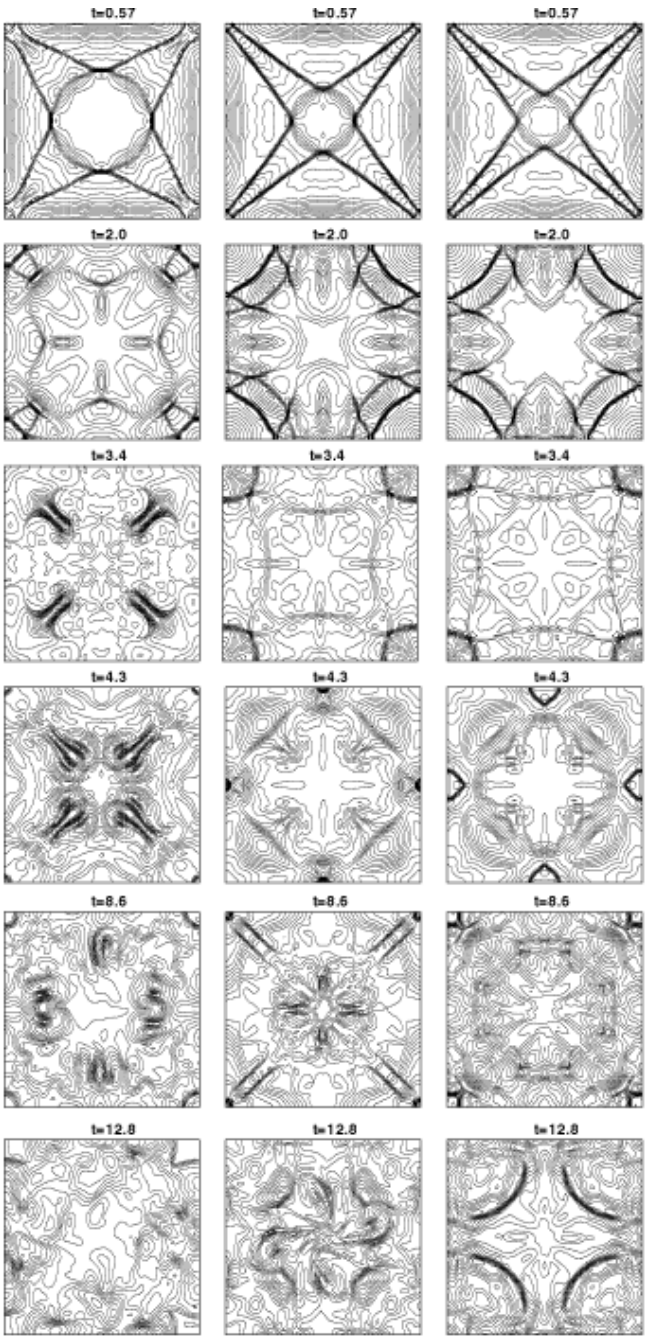


Figure 14. Mach number contours for symmetric blasts (case S) at three different Mach numbers: (*i*) left column $M_s = 2$, (*ii*) middle column $M_s = 5$, (*iii*) right column $M_s = 10$.

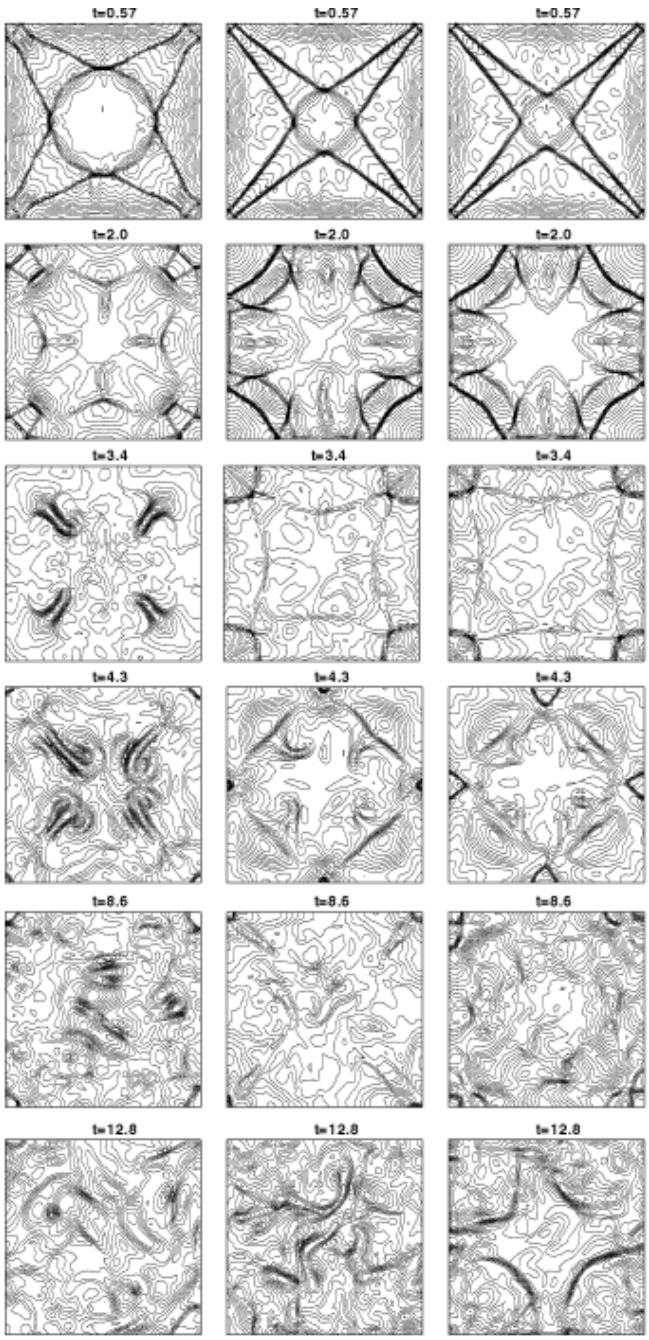


Figure 15. Mach number contours for perturbed blasts (case P1) at three different Mach numbers: (*i*) left column $M_s = 2$, (*ii*) middle column $M_s = 5$, (*iii*) right column $M_s = 10$.

later times. Yet, when increasing the Mach number, larger regions of positive vorticity appear as the simulation progresses. Finally, the combination of lower Mach number with strong perturbations leads to larger regions of negative vorticity.

3.6 Effects of shock instability on wall pressure distributions

The existence of the instability alters the geometrical symmetry of pressure distributions on the four walls and changes considerably the pressure values. Figures 20 and 21 show the wall pressure loads for $M_s = 2$ at two different time instants for the cases S, P1 and P2. The instability leads to different pressure distributions on the left, right, top and bottom walls of the enclosure. The perturbations lead to an enhancement of the wall-pressure asymmetries (as expected) but, additionally, they also result in larger wall-pressure loads.

The pressure loads for the unperturbed and perturbed cases of $M_s = 5$ and $M_s = 10$ at two different time instants are presented in Figs 22, 23, 24 and 25. Larger wall pressures, compared to $M_s = 2$, occur in this Mach number, which is due to the increased strength of the shock wave. Similar to $M_s = 2$, large differences in the pressure distributions on the four walls also occur between the perturbed and unperturbed cases. Increasing the perturbation amplitude results in

https://doi.org/10.1017/S0001924000000890 Published online by Cambridge University Press

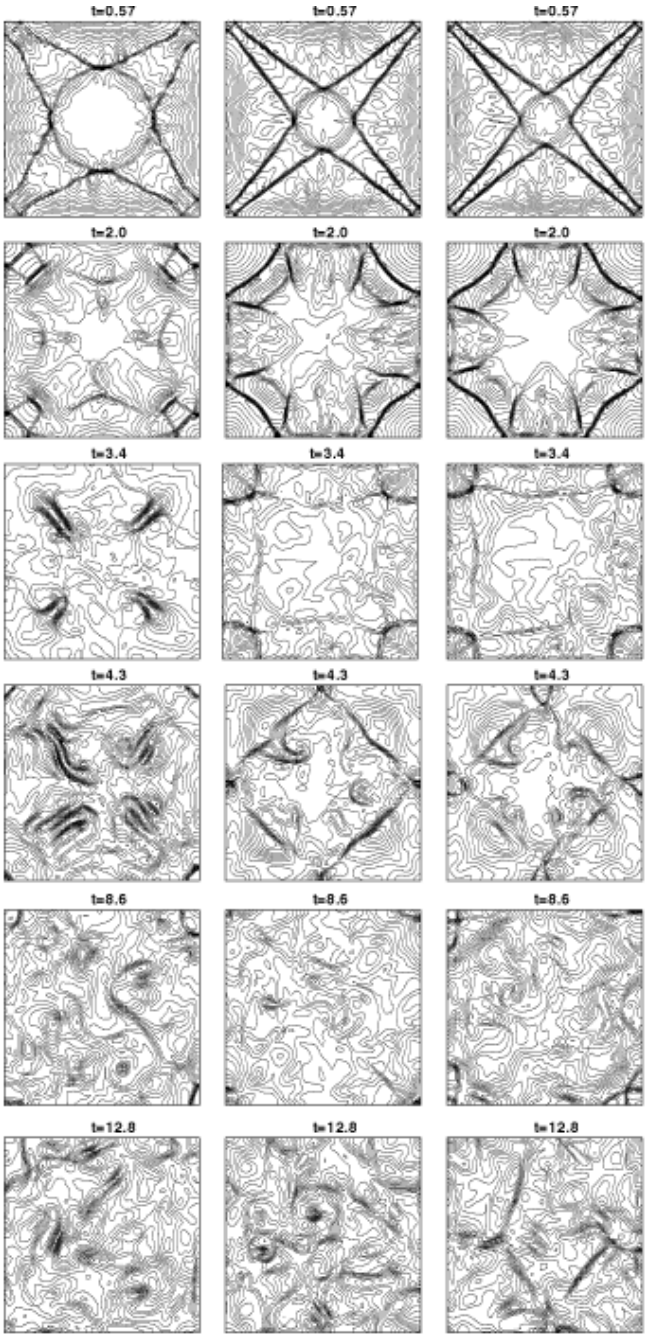


Figure 16. Mach number contours for perturbed blasts (case P2) at three different Mach numbers: (*i*) left column $M_s = 2$, (*ii*) middle column $M_s = 5$, (*iii*) right column $M_s = 10$.

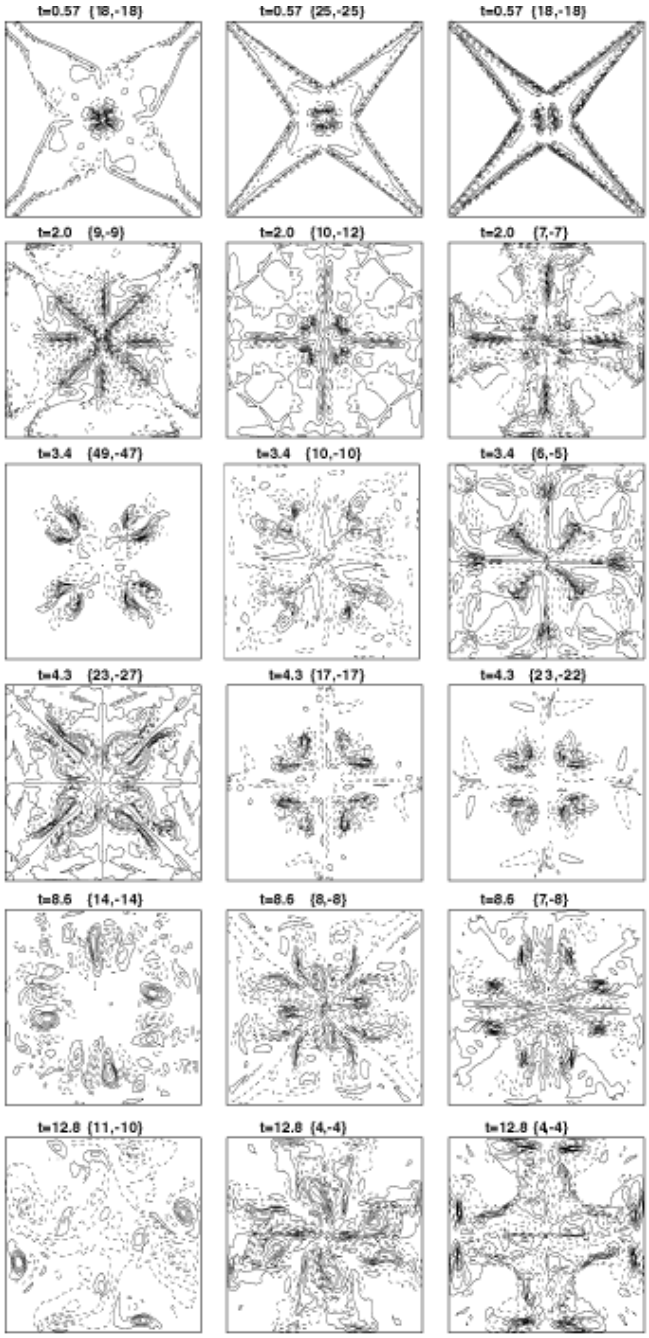


Figure 17. Vorticity contours for symmetric blasts (case S) at three different Mach numbers: left column $M_s = 2$, (*ii*) middle column $M_s = 5$, (*iii*) right column $M_s = 10$.; dashed lines denote negative vorticity.

larger wall pressures compared to the unperturbed flow (case *S*). Moreover, this effect is stronger with increased Mach number.

The overall maximum value of the wall-pressure, appearing over the entire duration of the blast propagation, is not significantly affected by the perturbations in the initial condition. For example, at $M_s = 2$ the maximum wall pressures are 1·66, 1·69 and 1·88 (MPa) for the cases S, P1 and P2, respectively, while at $M_s = 10$ the corresponding values are 116, 113 and 107 (MPa) for the three cases, respectively. Thus, for $M_s = 2$ the perturbation P2 increases the maximum pressure by a factor of 1·13 but, on the other hand, for $M_s = 10$ the same perturbation slightly decreases the maximum pressure by a factor of 0·92. The above can be explained bearing in mind that the overall maximum pressure appears at the early stages of the flow development, during the second reflection, where large asymmetries have not yet been established and, as a result, the effects of perturbations are less profound.

4.0 CONCLUSIONS

An investigation of shock-wave induced instability arising from an internal explosion in an enclosure was presented. The instability and

https://doi.org/10.1017/S0001924000000890 Published online by Cambridge University Press

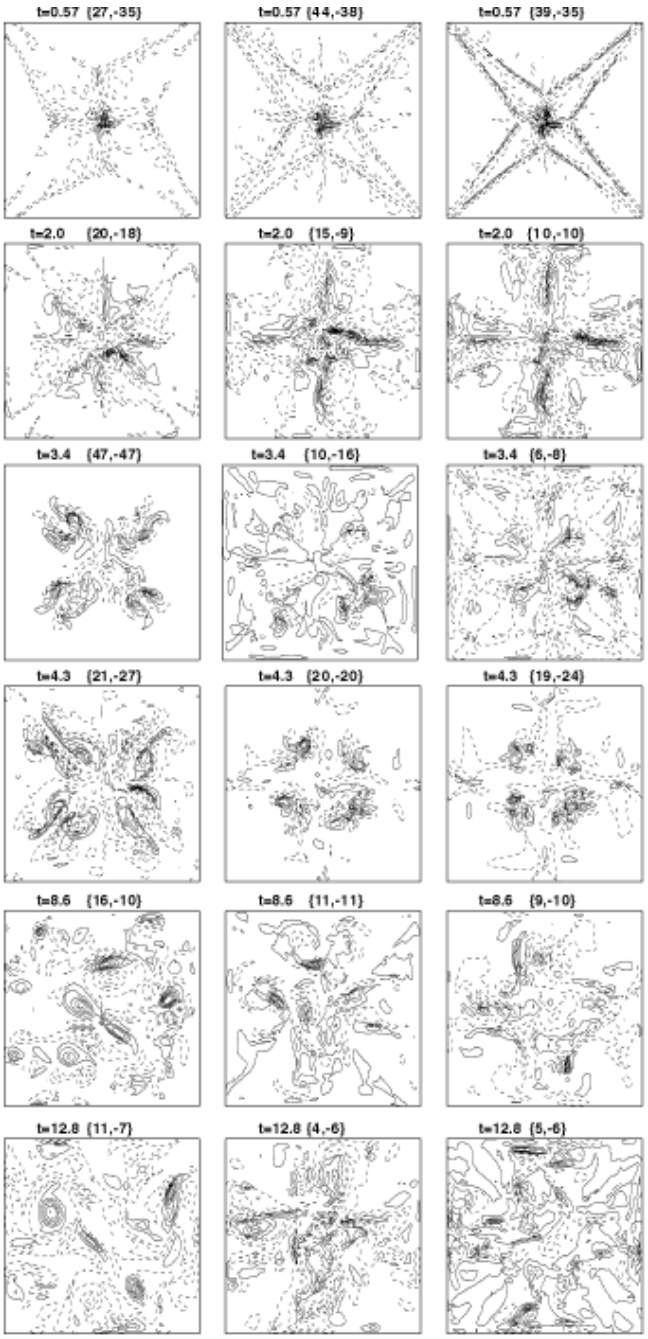


Figure 18. Vorticity contours for symmetric blasts (case P1) at three different Mach numbers: left column $M_s = 2$, (*ii*) middle column $M_s = 5$, (*iii*) right column $M_s = 10$. ; dashed lines denote negative vorticity.

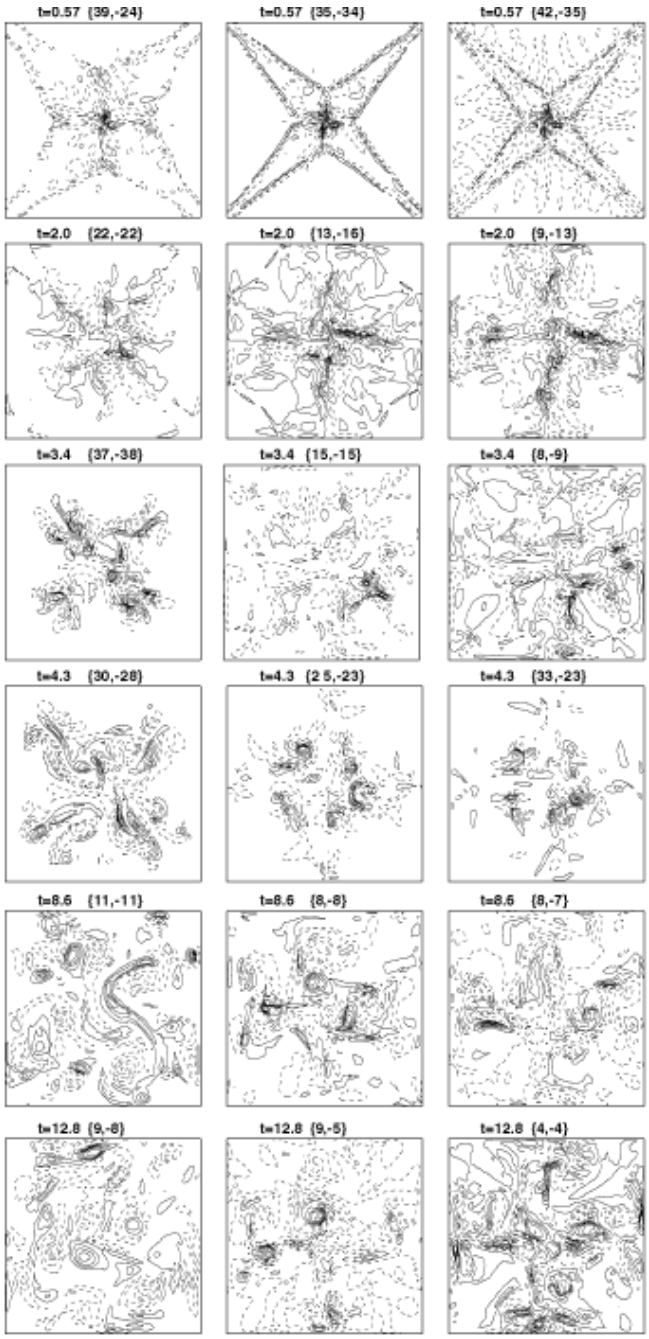


Figure 19. Vorticity contours for symmetric blasts (case P2) at three different Mach numbers: left column $M_s = 2$, (*ii*) middle column $M_s = 5$, (*iii*) right column $M_s = 10$.; dashed lines denote negative vorticity.

associated flow phenomena were studied at three different Mach numbers for both symmetric and perturbed blast waves. The computations revealed that the instability is manifested as a symmetry-breaking of the flow. The onset of the symmetry-breaking can be attributed to a Richtmyer-Meshkov instability initiating at the early stages of the flow development, particularly during the interaction of the shock waves reflected from the walls with the low density region in the centre of the enclosure. The phenomena observed in the present case share similarities with the Richtmyer-Meshkov instability occurring during the interaction of shock waves with gas inhomogeneities.

The instability initiates near the centre of the enclosure and the symmetric-breaking spreads fast throughout the flow field as a result of the multiple shock reflections. The formation of the instability is also associated with large positive and negative vorticity regions. These regions appear initially as elongated pairs of positive-negative vorticity, which take a circular form as the flow further evolves. The circular structures seem to be associated with more unstable regions and weakening of the shock waves. As a result, they appear earlier at lower Mach numbers and also become more evident under the presence of random perturbations in the initial field. For stronger shock waves, the flow field shows a tendency to be restabilised

https://doi.org/10.1017/S0001924000000890 Published online by Cambridge University Press

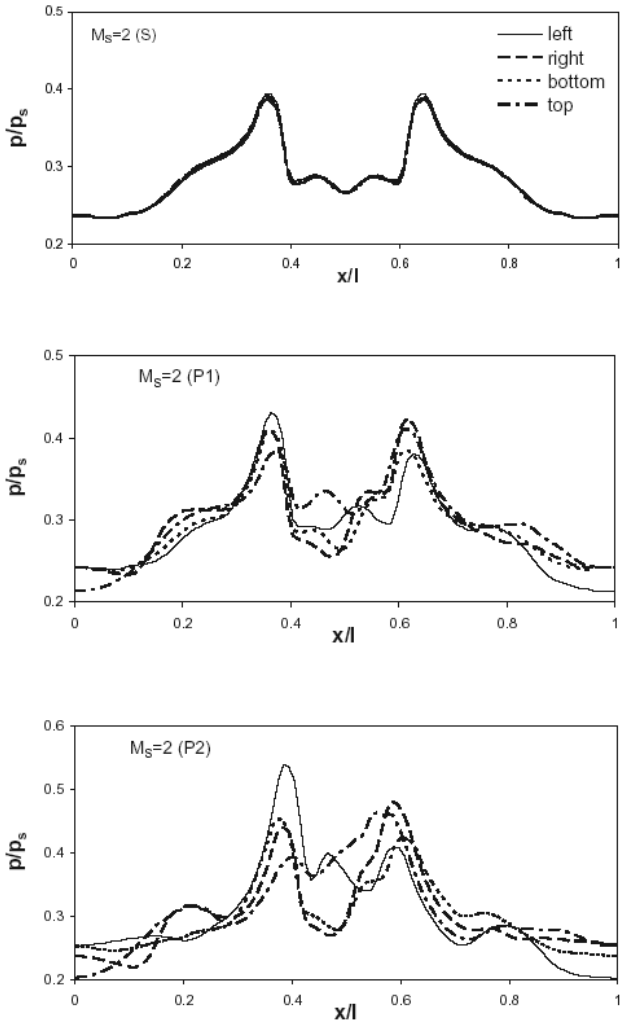


Figure 20. Wall pressure distributions for $M_s = 2$ at $t = 3{\cdot}42$ for the cases S, P1 and P2. The pressure values have been normalised to the shock wave pressure, p_s. The length becomes dimensionless using the box length, l.

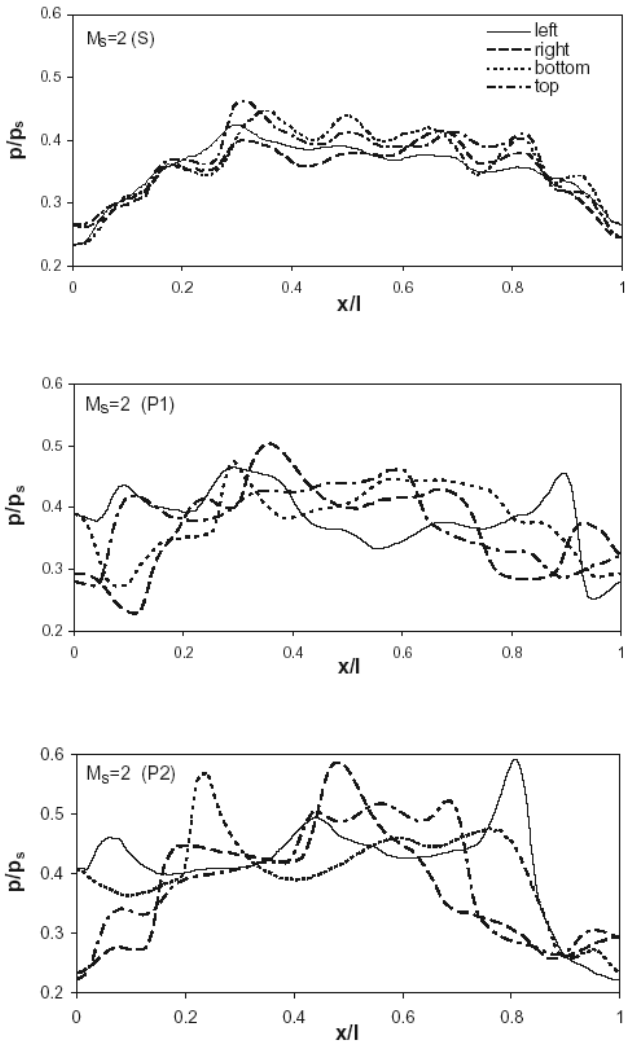


Figure 21. Wall pressure distributions for $M_s = 2$ at $t = 10{\cdot}27$ at for the cases S, P1 and P2. The pressure values have been normalised to the shock wave pressure, P_s. The length becomes dimensionless using the box length, l.

(turning to symmetry) after the onset of the instability and this effect lasts longer for $M_s = 10$ than $M_s = 5$, while it does not appear at all for $M_s = 2$. However, in all cases the flow becomes unstable at later times. The shock waves attenuate slower for higher Mach numbers, while the flow field is more prone to developing the instability in the case of a weaker blast.

The shock-wave induced instability also alters the wall pressure loads. The pressure distributions are not distributed symmetrically along the four walls. It was found that random perturbations imposed on the initial blast increase the instantaneous wall pressures. Therefore, the assumption of an unperturbed blast, commonly used in numerical simulations, should be avoided since this leads to an underestimation of the instantaneous pressure loads. However, the perturbations have small effects on the maximum value of the wall pressure occurring throughout the simulation.

REFERENCES

1. BAGABIR, A. and DRIKAKIS, D. Numerical experiments using high-resolution schemes for unsteady, inviscid, compressible flows, *Computer Methods in Applied Mechanics and Engineering*, 2004, **193**, (42-44), pp 4675-4705.
2. BAGABIR, A. and DRIKAKIS, D. Mach number effects on shock-bubble interaction. *Shock Waves J*, 2001, **11**, pp 209-218.
3. BEN-DOR, G. *Shock Wave Reflection Phenomena*, Springer-Verlag, 1992.
4. BOOK, D.L. Convective instability of self-similar spherical expansion into a vacuum. *J Fluid Mech,* 1979, **95**, pp 779-786.
5. Burrows, A. and FRYXELL B.A. An instability in neutron stars at birth. Science, 1992, **258**, pp 430-434.
6. CHEBOTAREVA, E.I., ALESHIN, A.N., ZAYTSEV, S.G. and SERGEEV, S.V. Investigation of interaction between reflected shocks and growing perturbation on an interface. *Shock Waves, 1999,* **9**, pp 81-86.
7. DAVYDOV, A.N., LEBEDEV, E.F. and PERKOV, S.A. Experimental investigation of gasdynamic instability in the plasma flow following the cylindrical shock wave. Preprint N1-40, Inst of High Temperatures, USSR, 1979.
8. DEWEY, J.M. Mach reflection research-paradox and progress, in: Takayama (Ed)., Proceedings of the 18th International Symposium on Shock Waves, Sendai, Japan (Springer-Verlag, 1992) pp 113-120.
9. DRIKAKIS, D. and DURST, F. A numerical study of viscous supersonic

https://doi.org/10.1017/S0001924000000890 Published online by Cambridge University Press

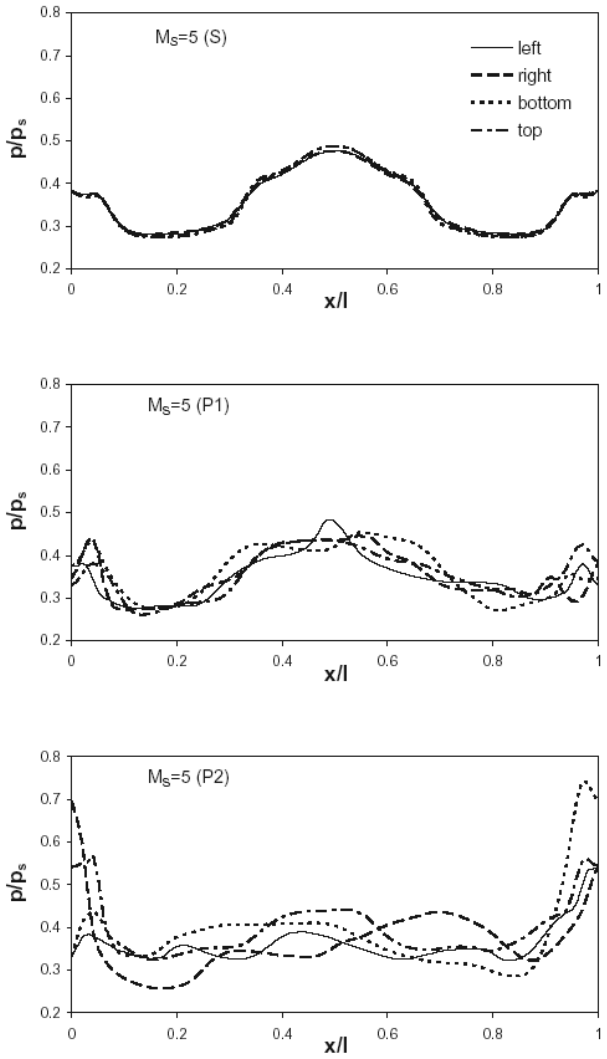


Figure 22. Wall pressure distributions for $M_s = 5$ at $t = 5{\cdot}7$ at for the cases S, P1 and P2. The pressure values have been normalised to the shock wave pressure, P_s. The length becomes dimensionless using the box length, l.

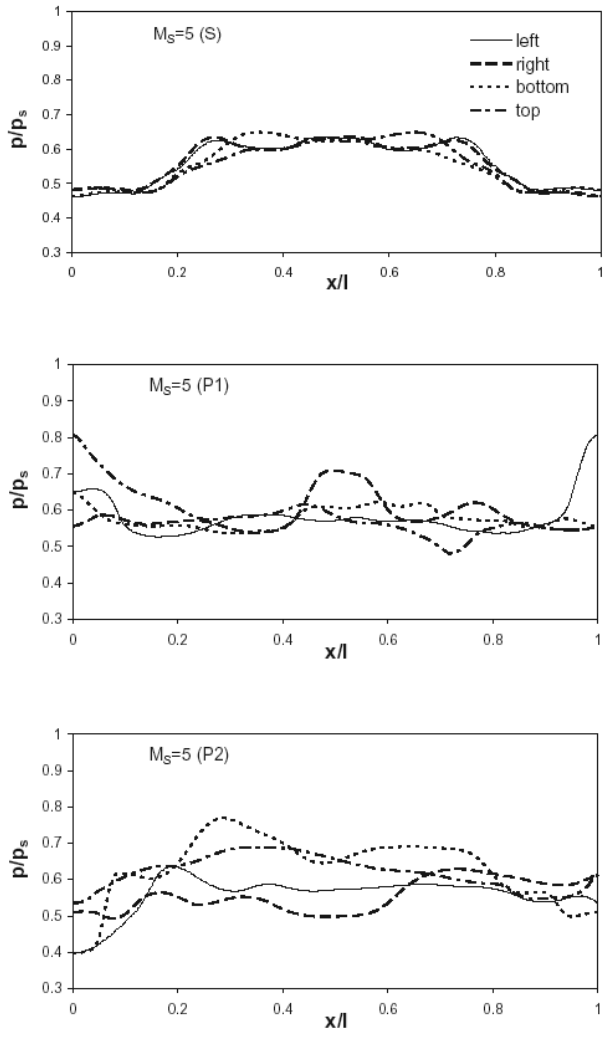


Figure 23. Wall pressure distributions for $M_s = 5$ at $t = 14{\cdot}26$ at for the cases S, P1 and P2. The pressure values have been normalised to the shock wave pressure, P_s. The length becomes dimensionless using the box length l.

flow past a flat plate at large angles of incidence. *Phys Fluids*, 1994, **6**, pp 1553-1573.

10. EBERLE, A. and HEISS, S. Enhanced numerical inviscid and viscous fluxes for cell centered finite volume schemes. *Computers and Fluids*, 1993, **22**, pp 295-309.
11. EINFELDT, B. On Godunov-type methods for gas dynamics. *SIAM J. Numer Anal*, 1988, **25,** pp 294-318.
12. HARTEN, A., LAX, P.D. and VAN LEER, B. On upstream differencing and Godunov-type schemes for hyperbolic conservation laws. *SIAM Review*, 1983, **25**, pp 35-61.
13. HOUAS, L., FARHAT, A. and BRUN, R. Shock induced Rayleigh-Taylor instability in the presence of a boundary layer. *Phys Fluids, 1988,* **31**.
14. MANKA, C., GRUN, J., STAMPER, J., RESNICK, J., BURRIS, R., CRAWFORD, J. and RIPIN, B.H. Images of unstable Taylor-Sedov blast waves propagating through a uniform gas. IEEE Transactions on Plasma Science 1996, **24**, pp 35-36.
15. MARCONI, F. Investigation of the interaction of a blast wave with an internal structure. *AIAA J*, 1994, **32**, pp 1561-1567.
16. ROE P.L. Approximate Riemann solvers, parameter vectors and difference schemes. *J Comput Phys,* 1981, **43**, pp 357-372.
17. ROE P.L. AND PIKE, J. Efficient construction and utilisation of approximate Riemann solutions. In: Proc of IMA conference on numerical methods in fluid dynamics, Computing Methods in Science and Engineering VI, 1984, North-Holland, INRIA.
18. RUPERT, V. Shock-interface interaction: current research on the Richtmyer-Meshkov problem. In: Proc of the 18th Int Symp on Shock Waves, 1991, Sendai, Japan.
19. SAKURAI A. *Blast Wave Theory. In: Basic Developments in Fluid Dynamics*, HOLT, M. (Ed), Academic Press, 1965, New York.
20. TAKAYAMA, K. *Optical Flow Visualisation of Shock Wave Phenomena*, BRUN and DIMITRESCU (Eds), Shock Waves at Marseille, Springer-Verlag, 1995, **4**, pp 7-16.
21. TORO, E.F. SPRUCE, M. and SPEARES, W. Restoration of the contact surface in the HLL-Riemann solver. Shock Waves, 1994, **4**, pp 25-34.
22. TORO, E.F *Riemann Solvers and Numerical Methods for Fluid Dynamics*, Springer Verlag, 1999.
23. THOMAS, J.L. and VAN LEER, WALTERS B. Implicit flux split scheme for the Euler equations. AIAA-paper 85-1680, 1985.
24. VAN ALBADA, G.D., VAN LEER, B. and ROBERTS, W. A comparative study of computational methods in cosmic gas dynamics, *Astron. Astrophys*, 1982, **108**.
25. ZOLTAK, J. and DRIKAKIS, D. Hybrid upwind methods for the simulation of unsteady shock-wave diffraction over a cylinder. *Comput Meth Appl Mech Eng*, 1998, **162**, pp 165-185.

https://doi.org/10.1017/S0001924000000890 Published online by Cambridge University Press

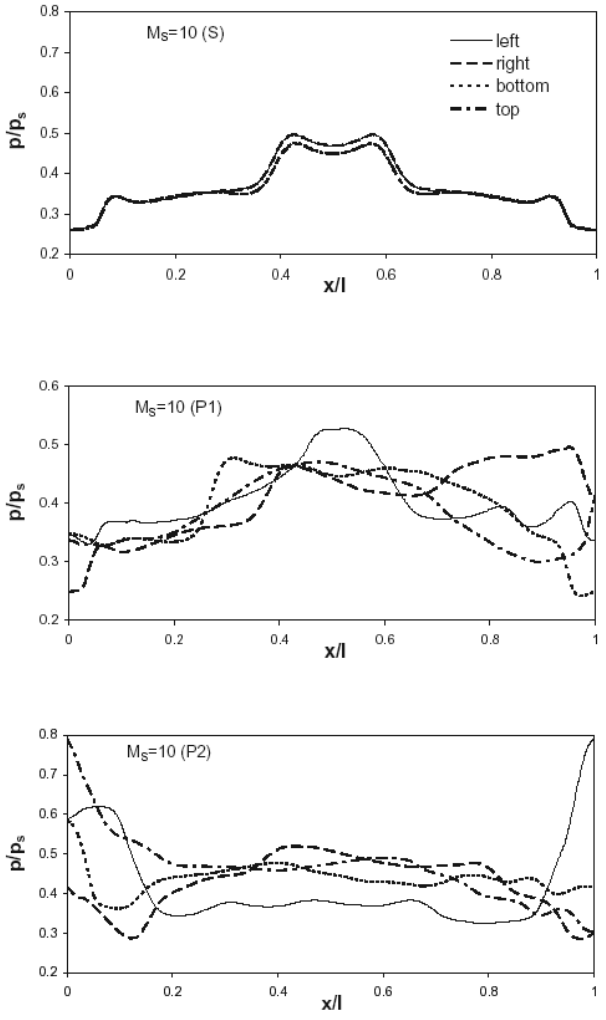


Figure 24. Wall pressure distributions for M_s = 10 at t = 8·56 at for the cases S, P1 and P2. The pressure values have been normalised to the shock wave pressure, P_s. The length becomes dimensionless using the box length l.

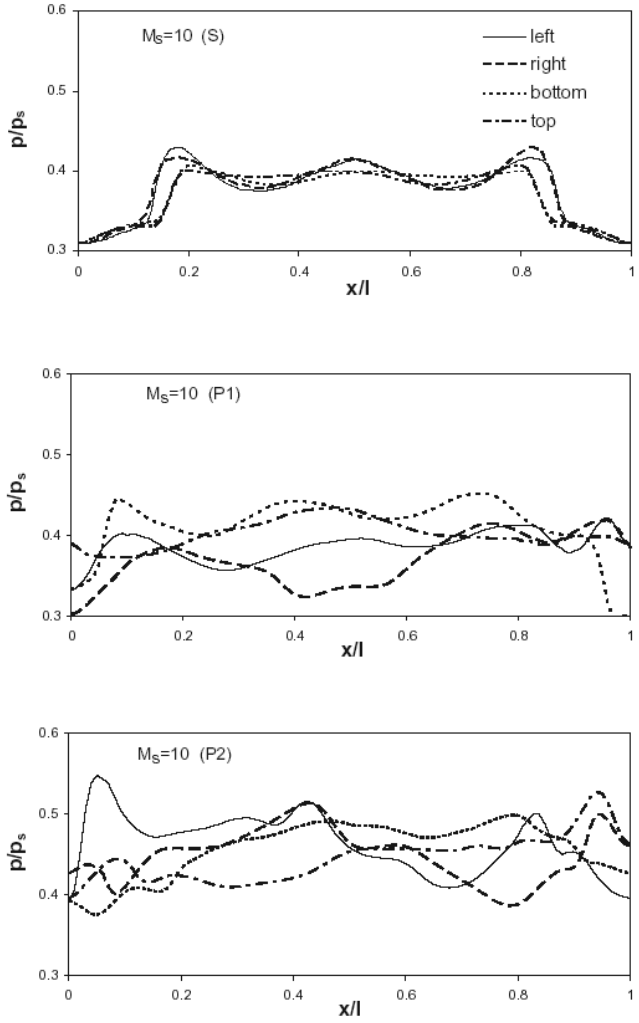


Figure 25. Wall pressure distributions for M_s = 10 at t = 14·26 at for the cases S, P1 and P2. The pressure values have been normalised to the shock wave pressure, P_s. The length becomes dimensionless using the box length l.

A1 APPENDIX: COMPUTATIONAL METHODS

A1.1 Roe's Riemann solver

Detailed description of this scheme can be found in the papers of Roe (1981) as well as of Roe and Pike (1984). Here, the Roe's flux is employed in the form;

$$E_{i+1/2} = \frac{1}{2}(E_L + E_R) - \frac{1}{2}\sum_{i=1}^{4}\tilde{\alpha}_i \left|\tilde{\lambda}_i\right| \tilde{K}^{(i)} \qquad \ldots (5)$$

where E_L and E_R are the left and right fluxes, $\tilde{\alpha}_i$ and $\tilde{\lambda}_i$ are the wave strengths and eigenvalues, respectively, and $\tilde{K}^{(i)}$ are the right eigenvectors. All the above are calculated using Roe's average[16].

A1.2 HLLC Riemann solver

The HLLC Riemann solver[21] is an improved variant of the HLL Riemann solver of Harten *et al*.[12]. The HLLC scheme considers two averaged intermediate states, U_L^* and U_R^*, seperated by the contact wave of speed S_m. The two-state approximate Riemann solutions are defined by;

$$\mathbf{U}_{\mathbf{HLLC}} = \begin{cases} U_L \ if & S_L > 0 \\ U_L^* \ if & S_L \le 0 < S_M \\ U_R^* \ if & S_M \le 0 \le S_R \\ U_R^* \ if & S_R < 0 \end{cases} \qquad \ldots (6)$$

and the corresponding interface flux is written as;

$$\mathbf{E}_{\mathbf{HLLC}} = \begin{cases} E_L \ if & S_L > 0 \\ E_L^* \ if & S_L \le 0 < S_M \\ E_R^* \ if & S_M \le 0 < S_R \\ E_R \ if & S_R < 0 \end{cases} \qquad \ldots (7)$$

Toro *et al*. (1994)[21] presented an approach for computing the 'star' states by assuming constant contact-wave speed S_M. Applying the Rankine-Hugoniot conditions across the acoustic waves of speeds S_L and S_R, gives;

https://doi.org/10.1017/S0001924000000890 Published online by Cambridge University Press

$$E_L^* = E_L + S_L\,(U_L^* - U_L) \quad \ldots (8)$$

$$E_R^* = E_R + S_R\,(U_R^* - U_R) \quad \ldots (9)$$

Equations (8) and (9) can be expressed as

$$S_L U_L^* - E_L^* = S_L U_L - E_L \quad \ldots (10)$$

$$S_R U_R^* - E_R^* = S_R U_R - E_R \quad \ldots (11)$$

Note that the right-hand side of Equations (10) and (11) is known. To determine U_L^* and U_R^*, Toro *et al* (1994)[21] assumed that $\lambda_{0,L}^* = \lambda_{0,R}^* = S_M$ where S_M can be estimated by the right and left states. Subsequently, Equations (10) and (11) can be manipulated to give the left ($K = L$) and right ($K = R$) states U_K^* and the corresponding fluxes as;

$$\mathbf{U}_\mathbf{K}^* = \begin{pmatrix} \rho_K^* \\ (\rho u)_K^* \\ (\rho w)_K^* \\ e_K^* \end{pmatrix} =$$

$$\frac{1}{S_K - S_M}\begin{pmatrix} \rho_K (S_K - \lambda_{0,K}) \\ \rho u_K (S_K - \lambda_{0,K}) + (p^* - p_k)\tilde{\xi}_x \\ \rho w_K (S_K - \lambda_{0,K}) + (p^* - p_k)\tilde{\xi}_z \\ e_K (S_K - \lambda_{0,K}) + p^* S_K - p_K \lambda_{0,k} \end{pmatrix} \quad \ldots (12)$$

$$\mathbf{E}_\mathbf{K}^* = J\,|\nabla\xi|\begin{pmatrix} \rho_K^* S_M \\ (\rho u)_K^* S_M + p^*\tilde{\xi}_x \\ (\rho w)_K^* S_M + p^*\tilde{\xi}_z \\ (\rho_K^* + p^*) S_M \end{pmatrix} \quad \ldots (13)$$

with;

$$p^* = \rho_K (\lambda_{0,K} - S_K)(\lambda_{0,K} - S_M) + p_K \quad \ldots (14)$$

The acoustic wave speeds $\mathbf{S_L}$ and $\mathbf{S_R}$ are taken from Einfeldt (1988):

$$\mathbf{S_L} = \min\left(\lambda_{0,L} - s, \tilde{\lambda} - \tilde{s}\right) \quad \ldots (15)$$

$$\mathbf{S_R} = \min\left(\lambda_{0,R} + s, \tilde{\lambda} + \tilde{s}\right) \quad \ldots (16)$$

where $\tilde{\lambda}$ and $\tilde{s}$ are Roe-average particle and sound speeds, respectively, and S_M is given in Einfeldt (1988):

$$\mathbf{S_M} = \frac{\rho_R \lambda_{0,R}(S_R - \lambda_{0,R}) - \rho_L \lambda_{0,L}(S_L - \lambda_{0,L}) + p_L - p_R}{\rho_R (S_R - \lambda_{0,R}) - \rho_L (S_L - \lambda_{0,L})} \quad \ldots (17)$$

A1.3 CBM-FVS scheme

The CBM (Characteristics-Based Method)-FVS (Flux Vector Splitting) scheme is a hybrid Riemann solver. The discretisation of the inviscid fluxes is obtained by a combination of a Riemann solver[10] and a FVS scheme[25,2]. The fluxes at the cell faces are defined by;

$$E = \tilde{\xi} E_{FVS} + (1 - \tilde{\xi}) E_{CBM} \quad \ldots (18)$$

The limiter $\tilde{\xi}$ is defined as

$$\tilde{\xi} = \min[1, a(1 - \min(f_i, f_{i+1}))|\mathbf{M}_{i+1} - \mathbf{M}_i|^2] \quad \ldots (19)$$

where M is the local Mach number. The coefficient $\boldsymbol{a}$ takes the value of 1 or 2 in hypersonic flows. The introduction of the FVS scheme acts as an additional numerical dissipation and is required only in the case of hypersonic Mach numbers and only in those regions where the CBM does not provide sufficient numerical dissipation to capture strong shock waves. The FVS scheme can be switched off, if a is set equal to 0. The term f_i is the van Albada limiter[24] given by:

$$\mathbf{f_i} = \max\left(0, \frac{2\nabla U_i \Delta U_i}{(\nabla U_i)^2 + (\Delta U_i)^2 + \epsilon}\right) \quad \ldots (20)$$

where $\nabla U_i = U_i - U_{i-1}$ and $\Delta U_i = U_{i+1} - U_i$, and ϵ is a small positive number preventing division by zero.

For the flux E_{FVS} a modified version of the Steger and Warming FVS scheme[25] has been employed. For this scheme the fluxes are given by;

$$\mathbf{E_{FVS}} = E^+ + E^- \quad \ldots (21)$$

$$\mathbf{E}^\pm = \rho J \nabla\xi \begin{pmatrix} \frac{1}{2}(\lambda_1^\pm + \lambda_2^\pm) \\ \left(u + \frac{s\tilde{\xi}_x}{\gamma}\right)\frac{\lambda_1^\pm}{2} + \left(u - \frac{s\tilde{\xi}_x}{\gamma}\right)\frac{\lambda_2^\pm}{2} \\ \left(w + \frac{s\tilde{\xi}_x}{\gamma}\right)\frac{\lambda_1^\pm}{2} + \left(w - \frac{s\tilde{\xi}_x}{\gamma}\right)\frac{\lambda_2^\pm}{2} \\ \frac{1}{2}H^\pm(\lambda_1^\pm + \lambda_2^\pm) \end{pmatrix} \quad \ldots (22)$$

where the split eigenvalues $\lambda_1^\pm$ and $\lambda_2^\pm$ are;

$$\lambda_1^\pm = \frac{\lambda_1 \pm |\lambda_1|}{2}, \lambda_2^\pm = \frac{\lambda_2 \pm |\lambda_2|}{2} \quad \ldots (23)$$

and the eigenvalues $\lambda_1^\pm$ and $\lambda_2^\pm$, are given by;

$$\lambda_1 = \lambda_0 + s, \lambda_2 = \lambda_0 - s \quad \ldots (24)$$

where $\boldsymbol{s}$ is the speed of sound and λ_0 is the streamline eigenvalue:

$$\lambda_0 = u\tilde{\xi}_x + w\tilde{\xi}_z \quad \ldots (25)$$

The metrics $\tilde{\xi}_x$ and $\tilde{\xi}_z$ are calculated by;

$$\tilde{\xi}_x = \frac{\xi_x}{\sqrt{\xi_x^2 + \xi_z^2}}, \tilde{\xi}_z = \frac{\xi_z}{\sqrt{\xi_x^2 + \xi_z^2}} \quad \ldots (26)$$

The above FVS version has been extensively validated in the past for various compressible flow problems[1,2,9,25].

The flux E_{CBM} is calculated according to Eberle's Riemann solver[10]:

$$\mathbf{E_{CBM}} = J\begin{pmatrix} \langle\rho u\rangle\xi_x + \langle\rho w\rangle\xi_z \\ \langle\rho u\rangle(\langle\rho u\rangle\xi_x + \langle\rho w\rangle\xi_z)/\langle\rho\rangle + \langle\rho\rangle\xi_x \\ \langle\rho w\rangle(\langle\rho u\rangle\xi_x + \langle\rho w\rangle\xi_z)/\langle\rho\rangle + \langle\rho\rangle\xi_z \\ (\langle e\rangle + \langle p\rangle)(\langle\rho u\rangle\xi_x + \langle\rho w\rangle\xi_z) \end{pmatrix} \quad \ldots (27)$$

where the average variables <ρ>, <ρ*u*>, <ρ*w*>,<*e*> are given by;

$$\langle\rho\rangle = \rho_0 + r_1 + r_2 \quad \ldots (28)$$

$$\langle\rho u\rangle = (\rho u)_0 + (u + s\xi_x)r_1 + (u - s\xi_x)r_2 \quad \ldots (29)$$

https://doi.org/10.1017/S0001924000000890 Published online by Cambridge University Press

$$\langle \rho w \rangle = (\rho w)_0 + (w + s\xi_z) r_1 + (w - s\xi_z) r_2 \quad \ldots (30)$$

$$\langle e \rangle = e_0 + (h + s\lambda_0) r_1 + (H - s\lambda_0) r_2 \quad \ldots (31)$$

with;

$$r_1 = \frac{1}{2s^2}\left(\left[\frac{\gamma - 1}{2}\left(u^2 + w^2\right) - s\lambda_0 \right](\rho_1 - \rho_0) \right.$$

$$+ [s\tilde{\xi}_x - (\gamma - 1)u][(\rho u)_1 - (\rho u)_0] + \quad \ldots (32)$$

$$\left. [s\tilde{\xi}_z - (\gamma - 1)w][(\rho w)_1 - (\rho w)_0] + (\gamma - 1)(e_1 - e_0) \right)$$

$$r_2 = \frac{1}{2s^2}\left(\left[\frac{\gamma - 1}{2}\left(u^2 + w^2\right) - s\lambda_0 \right](\rho_2 - \rho_0) \right.$$

$$+ [s\tilde{\xi}_x - (\gamma - 1)u][(\rho u)_2 - (\rho u)_0] + \quad \ldots (33)$$

$$\left. [s\tilde{\xi}_z - (\gamma - 1)w][(\rho w)_2 - (\rho w)_0] + (\gamma - 1)(e_2 - e_0) \right)$$

The variables denoted by the subscripts 0, 1 and 2 are the values on the corresponding characteristics, which are calculated by;

$$U_j = 0{\cdot}5[(1 + \eta_j)U_L + (1 - \eta_j)U_R], \; j = 0,1,2 \quad \ldots (34)$$

where;

$$\eta_j = 0{\cdot}5(3\beta - \beta^3)_j, \; \beta_j = [(\lambda_L + \lambda_R)/(|\lambda_L| + |\lambda_R|)]_j \quad \ldots (35)$$

High-resolution is obtained by the Monotone Upstream Scheme for Conservation Laws (MUSCL) scheme (see Thomas *et al* 1985[23] for details), which has been employed to calculate the left (U_L) and right (U_L) states of the conservative variables. This was implemented in conjunction with all three Riemann solvers considered in this work. Past validation studies of the CBM-FVS approach in unsteady flows with strong shock waves[25] have shown that the method provides accurate results comparable to those obtained by second-order accurate Godunov methods based on unstructured adaptive grids. Grid-adaptation was also considered in the framework of the present study, but as it has been pointed out[15], grid adaptation cannot be effective for the present problem due to the complexity of the shock interactions which lead to a chaotic-like flow field as the computation progresses.

A1.4 Time integration

The Riemann solvers presented above have been implemented in conjunction with an implicit-unfactored method second-order in time. At the time level $n + 1$ the Euler equations are written as;

$$J\frac{\alpha_{n+1}U^{n+1} - \alpha_n U^n + \alpha_{n-1}U^{n-1}}{\Delta t} + E_\xi^{n+1} + G_\varsigma^{n+1} = 0, \quad \ldots (36)$$

where

$$\alpha_{n+1} = 1 + 0{\cdot}5\theta, \; \alpha_n = 1 + \theta, \; \alpha_{n-1} = 0{\cdot}5\theta$$

The parameter θ defines the order of the time discretisation: θ = 0 and 1 for first- and second-order, respectively.

The fluxes E and G are linearised around the time level n:

$$E^{n+1} = E^n + A^n \Delta U \quad \ldots (37)$$

$$G^{n+1} = G^n + C^n \Delta U \quad \ldots (38)$$

where $\Delta U = U^{n+1} - U^n$ and $A = \frac{\partial E}{\partial U}, C = \frac{\partial G}{\partial U}$ are the Jacobians of the inviscid fluxes. Using the above linearisation, Equation (42) is written as:

$$J\frac{\alpha_{n+1}U^{n+1} - \alpha_n U^n + \alpha_{n-1}U^{n-1}}{\Delta t} + (A^n \Delta U)_\xi + (C^n \Delta U)_\zeta = -(E_\xi^n + G_\zeta^n) \quad \ldots (39)$$

A unfactored Newton-type method is constructed by defining a sequence of approximations q, between two time steps n and $n + 1$, such that;

$$\lim_{\nu > 1} q^\nu \to U^{n+1} \quad \ldots (40)$$

where ν stands for the Newton sub-iterations. Then, Equation (46) becomes;

$$J\frac{\alpha_{n+1}\Delta q^{\nu+1}}{\Delta t} + (A^\nu \Delta q^{\nu+1})_\xi + (C^\nu \Delta q^{\nu+1})_\varsigma =$$

$$-J\frac{\alpha_{n+1}\, q^\nu - \alpha_n U^n + \alpha_{n-1}U^{n-1}}{\Delta t} - RHS \quad \ldots (41)$$

where;

$$q^{\nu+1} = q^\nu + \Delta q^{\nu+1}, \; RHS = E_\xi^\nu + G_\varsigma^\nu \quad \ldots (42)$$

To obtain an implicit unfactored solution, Equation (47) is written for each cell (i,k) in the following form;

$$(DIAG)_{i,k}^\nu \, \Delta q_{i,k}^{\mu+1,\nu} = -\omega^* (TA + RHS)_{i,k}^\nu + (ODIAG)_{i,k}^\nu \quad \ldots (43)$$

where;

$$TA = J\frac{\alpha_{n+1}q^\nu - \alpha_n U^n + \alpha_{n-1}U^{n-1}}{\Delta t}$$

$(DIAG)_{i,k}^n$ is a 4×4 matrix containing the diagonal elements of the eigenvalue-split inviscid Jacobians and the term $\frac{I}{\Delta t}$, where I is the identity matrix. $(ODIAG)_{i,k}$ includes the off-diagonal elements and is a function of $\Delta U_{i+1,k}$, $\Delta U_{i-1,k}$, $\Delta U_{i,k+1}$, and $\Delta U_{i,k-1}$. The inversion of the above system of equations is performed by a point-by-point Gauss-Seidel relaxation. In the present computations four Gauss-Seidel steps ($\mu = 4$) and two Newton sub-iterations ($\nu = 2$) are used. The under-relaxation parameter ω^* is used to compensate for the different orders of accuracy between the left and right hand sides of the equations. The value of $\omega^* = 0{\cdot}6 - 0{\cdot}8$ has been used in this study.

https://doi.org/10.1017/S0001924000000890 Published online by Cambridge University Press